



**HAL**  
open science

## Kepler Object of Interest Network. I. First results combining ground- and space-based observations of Kepler systems with transit timing variations

C. von Essen, A. Ofir, S. Dreizler, E. Agol, J. Freudenthal, J. Hernández, S. Wedemeyer, V. Parkash, H. J. Deeg, S. Hoyer, et al.

### ► To cite this version:

C. von Essen, A. Ofir, S. Dreizler, E. Agol, J. Freudenthal, et al.. Kepler Object of Interest Network. I. First results combining ground- and space-based observations of Kepler systems with transit timing variations. *Astronomy and Astrophysics - A&A*, 2018, 615, 10.1051/0004-6361/201732483 . insu-03666267

**HAL Id: insu-03666267**

**<https://insu.hal.science/insu-03666267>**

Submitted on 12 May 2022

**HAL** is a multi-disciplinary open access archive for the deposit and dissemination of scientific research documents, whether they are published or not. The documents may come from teaching and research institutions in France or abroad, or from public or private research centers.

L'archive ouverte pluridisciplinaire **HAL**, est destinée au dépôt et à la diffusion de documents scientifiques de niveau recherche, publiés ou non, émanant des établissements d'enseignement et de recherche français ou étrangers, des laboratoires publics ou privés.

# Kepler Object of Interest Network<sup>★</sup>

## I. First results combining ground- and space-based observations of *Kepler* systems with transit timing variations

C. von Essen<sup>1,2</sup>, A. Ofir<sup>2,3</sup>, S. Dreizler<sup>2</sup>, E. Agol<sup>4,5,6</sup>, J. Freudenthal<sup>2</sup>, J. Hernández<sup>7</sup>, S. Wedemeyer<sup>8,9</sup>, V. Parkash<sup>10</sup>, H. J. Deeg<sup>11,12</sup>, S. Hoyer<sup>11,12,13</sup>, B. M. Morris<sup>4</sup>, A. C. Becker<sup>4</sup>, L. Sun<sup>14</sup>, S. H. Gu<sup>14</sup>, E. Herrero<sup>15</sup>, L. Tal-Or<sup>2,17</sup>, K. Poppenhaeger<sup>18</sup>, M. Mallonn<sup>19</sup>, S. Albrecht<sup>1</sup>, S. Khalafinejad<sup>20</sup>, P. Boumis<sup>21</sup>, C. Delgado-Correal<sup>22</sup>, D. C. Fabrycky<sup>23</sup>, R. Janulis<sup>24</sup>, S. Lalitha<sup>25</sup>, A. Liakos<sup>21</sup>, Š. Mikolaitis<sup>24</sup>, M. L. Moyano D'Angelo<sup>26</sup>, E. Sokov<sup>27,28</sup>, E. Pakštienė<sup>24</sup>, A. Popov<sup>29</sup>, V. Krushinsky<sup>29</sup>, I. Ribas<sup>15</sup>, M. M. Rodríguez S.<sup>7</sup>, S. Rusov<sup>27</sup>, I. Sokova<sup>27</sup>, G. Tautvaišienė<sup>24</sup>, and X. Wang<sup>14</sup>

(Affiliations can be found after the references)

Received 18 December 2017 / Accepted 9 February 2018

### ABSTRACT

During its four years of photometric observations, the *Kepler* space telescope detected thousands of exoplanets and exoplanet candidates. One of *Kepler*'s greatest heritages has been the confirmation and characterization of hundreds of multi-planet systems via transit timing variations (TTVs). However, there are many interesting candidate systems displaying TTVs on such long timescales that the existing *Kepler* observations are of insufficient length to confirm and characterize them by means of this technique. To continue with *Kepler*'s unique work, we have organized the “*Kepler* Object of Interest Network” (KOINet), a multi-site network formed of several telescopes located throughout America, Europe, and Asia. The goals of KOINet are to complete the TTV curves of systems where *Kepler* did not cover the interaction timescales well, to dynamically prove that some candidates are true planets (or not), to dynamically measure the masses and bulk densities of some planets, to find evidence for non-transiting planets in some of the systems, to extend *Kepler*'s baseline adding new data with the main purpose of improving current models of TTVs, and to build a platform that can observe almost anywhere on the northern hemisphere, at almost any time. KOINet has been operational since March 2014. Here we show some promising first results obtained from analyzing seven primary transits of KOI-0410.01, KOI-0525.01, KOI-0760.01, and KOI-0902.01, in addition to the *Kepler* data acquired during the first and second observing seasons of KOINet. While carefully choosing the targets we set demanding constraints on timing precision (at least 1 min) and photometric precision (as good as one part per thousand) that were achieved by means of our observing strategies and data analysis techniques. For KOI-0410.01, new transit data revealed a turnover of its TTVs. We carried out an in-depth study of the system, which is identified in the NASA Data Validation Report as a false positive. Among others, we investigated a gravitationally bound hierarchical triple star system and a planet–star system. While the simultaneous transit fitting of ground- and space-based data allowed for a planet solution, we could not fully reject the three-star scenario. New data, already scheduled in the upcoming 2018 observing season, will set tighter constraints on the nature of the system.

**Key words.** instrumentation: photometers – methods: data analysis – techniques: photometric – planets and satellites: dynamical evolution and stability

## 1. Introduction

Transit observations provide a wealth of information about alien worlds. In addition to the detection and characterization of exoplanets (e.g., Seager 2010), once an exoplanet is detected by its transits the variations in the observed mid-transit times can be used to characterize the dynamical state of the system (Holman & Murray 2005; Agol et al. 2005). The timings of a transiting planet can sometimes be used to derive constraints on the planetary physical and orbital parameters in the case of multiple transiting planets (Holman et al. 2010), to set constraints on the masses of the perturbing bodies (Ofir et al. 2014), and to characterize the mass and orbit of a non-transiting planet,

with masses potentially as low as an Earth mass (Agol et al. 2005; Nesvorný et al. 2013; Barros et al. 2014; Kipping et al. 2014; Jontof-Hutter et al. 2015). For faint stars, this is extremely challenging to achieve by means of other techniques.

In the past three decades, non-Keplerian motions of exoplanets have been regularly studied from the ground and space (Rasio et al. 1992; Malhotra et al. 1992; Peale 1993; Wolszczan 1994; Laughlin & Chambers 2001; Rivera et al. 2010; Holman et al. 2010; Lissauer et al. 2011a; Becker et al. 2015; Gillon et al. 2016). Some examples of ground-based transit timing variation (TTV) studies are WASP-10b (Maciejewski et al. 2011), WASP-5b (Fukui et al. 2011), WASP-12b (Maciejewski et al. 2013), and WASP-43b (Jiang et al. 2016). Accompanying the observational growth, theoretical and numerical models were developed to reproduce the timing shifts and to represent the most probable orbital configurations (e.g., Agol et al. 2005; Nesvorný & Morbidelli 2008; Lithwick et al. 2012;

<sup>★</sup> Ground-based photometry is only available at the CDS via anonymous ftp to [cdsarc.u-strasbg.fr](https://cdsarc.u-strasbg.fr) (130.79.128.5) or via <http://cdsarc.u-strasbg.fr/viz-bin/qcat?J+A+A/615/A79>

Deck et al. 2014). There is no doubt about the detection power of the TTV method: given the mass of the host star, analyzing photometric observations we can sometimes retrieve the orbital and physical properties of complete planetary systems (Carter et al. 2012). However, the method requires a sufficiently long baseline, precise photometry, and good phase coverage.

From ground-based studies, which have focused on TTVs of hot Jupiters, there have already been some discrepant results (see, e.g., Qatar-1, von Essen et al. 2013; Mislis et al. 2015; Collins et al. 2017), especially when small telescopes are involved and TTVs of low amplitude are being measured (von Essen et al. 2016). Also, many follow-up campaigns of hot Jupiters could not significantly observe TTVs from the ground (see, e.g., Steffen & Agol 2005; Fukui et al. 2016; Petrucci et al. 2015; Raetz et al. 2015; Mallonn et al. 2015, for TrES-1, HAT-P-14b, WASP-28b, WASP-14b, and HAT-P-12b, respectively). However, hot Jupiters tend to be isolated from companion planets (Steffen et al. 2012b) so it does not come as a surprise that these studies have not resulted in convincing signals. It was with the advent of space-based observatories that a new era in the TTV quest started. In March 2009, NASA launched the *Kepler* space telescope (Borucki et al. 2010; Koch et al. 2010). The main goal of the mission was to detect Earth-sized planets in the so-called habitable zone, orbiting around stars similar to our Sun. The wide field of view allowed simultaneous and continuous monitoring of many thousands of stars for about four years. Surprisingly, *Kepler* showed a bounty of planetary systems with a much more compact configuration than our solar system (Lissauer et al. 2014). About 20% of the known planetary systems present either more than one planet or more than one star (Fabrycky et al. 2014). Particularly, most multiple systems are formed by at least two planets, and about one-third of these appear to be close to mean motion resonant orbits (see Lissauer et al. 2011b). Thus, the long-term and highly precise observations provided by *Kepler* have been the most successful data source used to confirm and characterize planetary systems via TTVs. At the top of a very long list, the first example of outstanding TTV discoveries is Kepler-9 (Holman et al. 2010). Since then, several other planetary systems have been confirmed, detected, or even characterized by means of TTV studies (see, e.g., Hadden & Lithwick 2014; Nesvorný et al. 2014). Classic examples are Kepler-11 (Lissauer et al. 2011a), Kepler-18 (Cochran et al. 2011), Kepler-19 (Ballard et al. 2011), Kepler-23 and Kepler-24 (Ford et al. 2012a), Kepler-25 to Kepler-28 (Steffen et al. 2012a), Kepler-29 to Kepler-32 (Fabrycky et al. 2012), and Kepler-36 (Carter et al. 2012). The list goes up to Kepler-87 (Ofir et al. 2014) and continues with K2, *Kepler*'s second chance at collecting data that will allow us to investigate planetary systems by means of TTVs (see, e.g., Becker et al. 2015; Nespral et al. 2017; Jontof-Hutter et al. 2016; Hadden & Lithwick 2017). Mazeh et al. (2013) analyzed the first twelve quarters of *Kepler* photometry and derived the transit timings of 1960 *Kepler* objects of interest (KOIs). An updated analysis of *Kepler* TTVs using the full long-cadence data set can be found under Holczer et al. (2016). The authors found that 130 KOIs presented significant TTVs, either because their mid-transit times had a large scatter, showed a periodic modulation, or presented a parabola-like trend. Although ~80 KOIs showed a clear sinusoidal variation, for several other systems the periodic signal was too long in comparison with the time span of the *Kepler* data to cover one full TTV cycle. As a consequence, no proper dynamical characterization could be carried out.

To overcome this drawback and expand upon *Kepler*'s heritage, in the framework of a large collaboration we organized

the *Kepler* Object of Interest Network<sup>1</sup> (KOINet). The main purpose of KOINet is the dynamical characterization of selected KOIs showing TTVs. To date, the network is comprised of numerous telescopes and is continuously evolving. KOINet's first light took place in March 2014. Here we show representative data obtained during our first and second observing seasons that will highlight the need for KOINet. Section 2 shows the basic working structure of KOINet and the scientific milestones. Section 3 describes the observing strategy and the data reduction process. Section 4 makes special emphasis to the fitting strategy of both ground and space-based data. In Sect. 5 we show KOINet's achieved milestones, and we finish with Sect. 6, where we present our conclusions and a brief description of the future observing seasons of KOINet.

## 2. *Kepler* Object of Interest Network

### 2.1. Rationale

The unique characteristic of KOINet is that it uses already existing telescopes, coordinated to work together towards a common goal. The data collected by the network will provide three major contributions to the understanding of the exoplanet population. First, deriving planetary masses from transit timing observations for more planets will populate the mass-radius diagram. The distribution of planetary radii at a given planetary mass is surprisingly wide, revealing a large spread in internal compositions (see, e.g., Mordasini et al. 2012). New mass and radius determinations will provide new constraints for planet structure models. Furthermore, longer transit monitoring will set tighter constraints on the existence of non-transiting planets (Barros et al. 2014), providing a broader and deeper view of the architecture of planetary systems. Finally, a larger sample of well-constrained physical parameters of planets and planetary systems will provide better constraints for their formation and evolution (Lissauer et al. 2011b; Fang & Margot 2012).

Initially, KOINet is focusing its instrumental resources on 60 KOIs that require additional data to complete a proper characterization or validation by means of the TTV technique. Basic information on the selected KOIs can be seen in the left part of Table 2. The KOI target list was built up based on the work of Ford et al. (2012b), Mazeh et al. (2013), Xie (2013, 2014), Nesvorný et al. (2013), Ofir et al. (2014), and Holczer et al. (2016). The 60 KOIs were drawn from four groups, depending on the scientific insights that further observations were expected to provide.

For a pair of planets, an anti-correlation in the TTV signal is expected to occur. This is the product of conservation of energy and angular momentum and is stronger when the planetary pair is near mean-motion resonance (see, e.g., Holman et al. 2010; Carter et al. 2012; Lithwick et al. 2012). The systems that present polynomial-shaped TTVs and show anti-correlated TTV signals are given the highest priority, independent of their status as valid planet candidates. In these cases, any additional data points in their parabola-shaped TTVs can reveal a turnover point, allowing a more accurate determination of planetary masses. Further data will allow the analysis of the system's dynamical characteristics. The systems that present anti-correlation and a sinusoidal variation but are poorly sampled have second priority (e.g., KOI-0880.01/02; a detailed analysis of the system is in preparation). In this case, more data points will allow us to improve the dynamical analysis of these systems. Under

<sup>1</sup> [koinet.astro.physik.uni-goettingen.de](http://koinet.astro.physik.uni-goettingen.de)

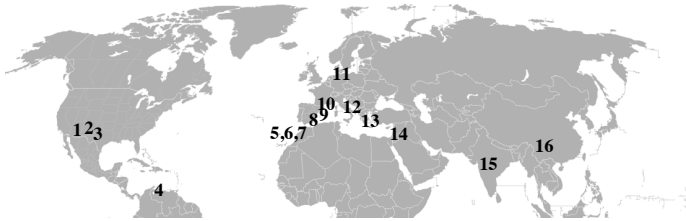


**Fig. 1.** Earth’s northern hemisphere, showing approximate locations of the observing sites that acquired data for KOINet during the 2014 and 2015 seasons (observatory names listed in Table 1).

third priority fall the KOIs with very long TTV periodicity. Additional data might shed some light onto the constitution of these systems (e.g., KOI-0525.01, Sect. 5.3). Finally, the lowest priority is given to those systems that have already been characterized and to the systems showing only one TTV signal (e.g., KOI-0410.01, Sect. 5.5). In this last group, under specific conditions the perturber’s mass and orbital period can be constrained, confirming or ruling out its planetary nature (e.g., Nesvorný et al. 2013, 2014).

## 2.2. Observing time

During the first two observing seasons (April–September 2014 and 2015) an approximate total of 600 h were collected for our project, divided between 16 telescopes and 139 observing events. Rather than following up all of the KOIs, we focused on the most interesting ones from a dynamical point of view. Here we present a general overview of the data collected by KOINet and its performance; we will focus in the analysis of individual KOIs in upcoming publications.

## 2.3. Basic characteristics of the KOINet telescopes

*Kepler* planets and planet candidates showing TTVs generally present two major disadvantages for ground-based follow-up observations. On the one hand, their host stars are relatively faint ( $K_p \sim 12$ –16). On the other hand, most of the KOIs reported to have large amplitude TTVs produce shallow primary transits. To collect photometric data with the necessary precision to detect shallow transits in an overall good cadence, most of KOINet’s telescopes have relatively large collecting areas. This allows data to be collected at a frequency of some seconds to a few minutes. Another observational challenge comes with the transit duration. For some of the KOIs the transit duration is longer than the astronomical night, especially bearing in mind that the *Kepler* field is best observable around the summer season when the nights are shorter. In these cases full transit coverage can only be obtained combining telescopes well separated in longitude. The telescopes included in this collaboration are spread across America, Europe, and Asia, allowing almost 24 h of continuous coverage. A world map including the telescopes that collected data during 2014 and 2015 can be found in Fig. 1 and Table 1.

Considering these two fundamental limitations, to maximize the use of KOINet data and boost transit detection, we have included the KOIs with transit depth larger than one part per thousand (ppt) and whose *Kepler* timing variability (i.e., the variability comprised within *Kepler* time span) is greater than two minutes (see Fig. 2). Below these limits, the photometric precision (and thus the derived timing precision) and especially the impact of correlated noise on photometric data

**Table 1.** Observatories that collected data during the 2014 and 2015 observing seasons.

1	Multiple Mirror Telescope Observatory (6.5 m), USA
2	Apache Point Observatory (3.5 m), USA
3	Monitoring Network of Telescopes (1.2 m), USA
4	Observatorio Astronómico Nacional del Llano del Hato (1 m), Venezuela
5	Nordic Optical Telescope (2.5 m), Spain
6	Liverpool Telescope (2 m), Spain
7	IAC80 telescope (0.8 m), Instituto de Astrofísica de Canarias, Spain
8	Calar Alto Observatory (1.25, 2.2, 3.5 m), Spain
9	Planetary Transit Study Telescope (0.6 m), Spain
10	Joan Oró Telescope – The Montsec Astronomical Observatory (0.8 m), Spain
11	Oskar Lühning Telescope – Hamburger Sternwarte (1.2 m), Germany
12	Bologna Astronomical Observatory (1.52 m), Italy
13	Kryoneri Observatory – National Observatory of Athens (1.2 m), Greece
14	Wise Observatory – Tel-Aviv University (1 m), Israel
15	IUCAA Girawali Observatory (2 m), India
16	Yunnan Observatories (2.4 m), PR China

**Notes.** The labels correspond to those of Fig. 1.

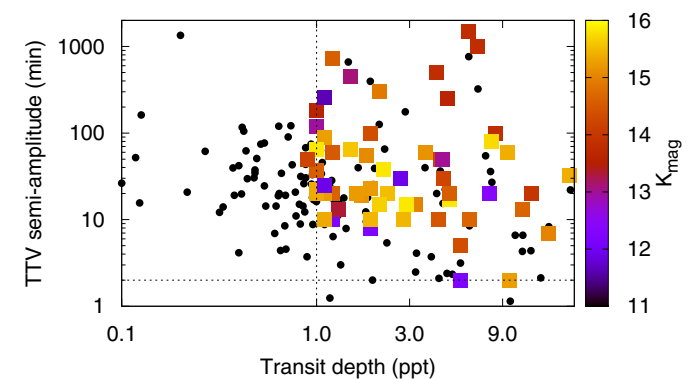


**Fig. 2.** *Kepler* TTV variability in minutes versus transit depth in ppt for the 60 KOIs that are included in KOINet (colored rectangles). The squares are color-coded depending on the *Kepler* magnitude of the host star. Black circles show all the KOIs presenting TTVs with a *Kepler* variability larger than 1 minute. Vertical and horizontal dashed lines indicate the  $\sim 1$  ppt and 2-min limits for KOINet.

(Carter & Winn 2009) would play a fundamental role in the detection of transit events. Next, we describe the primary characteristics of the telescopes involved in this work.

- The Apache Point Observatory, located in New Mexico, United States of America, hosts the Astrophysical Research Consortium 3.5-m telescope (hereafter ARC 3.5 m). The data were collected using Agile (Mukadam et al. 2011). The ARC 3.5m observed one transit of KOI-0525.01, our lower-limit KOI for transit depth. Nonetheless, during the first observing seasons we collected a substantial amount of data that will be presented in future work.
- The Nordic Optical Telescope (hereafter NOT 2.5 m) is located at the Roque de los Muchachos Observatory in La Palma, Spain, and belongs to the Nordic Optical Telescope Scientific Association, governed and funded by Scandinavian countries. In this work we present observations of KOI-0760.01 and KOI-0410.01.
- The 2.2 m Calar Alto Telescope (hereafter CAHA 2.2 m) is located in Almería, Spain. We observed KOI-0410.01 using the Calar Alto Faint Object Spectrograph in its photometric mode.
- The IAC80 telescope (hereafter IAC 0.8 m) is located at the Observatorio del Teide, in the Canary Islands, Spain. We observed half a transit of KOI-0902.01 for about 7 h.

- The Lijiang 2.4 m telescope (hereafter YO 2.4 m) is located at the Yunnan Observatories in Kunming, PR China. In this work we present observations of KOI-0410.01.

## 2.4. Maximizing the use of KOINet's time

### 2.4.1. Assigning telescopes to KOIs

In order to effectively distribute the available telescope time and maximize our chances of detecting transit events, three main characteristics have to be considered: the apparent magnitude of the host star, the available collecting area given by the size of the primary mirror, and the amplitude and scatter of *Kepler* TTVs. With the main goal of connecting the KOIs to the most suitable telescopes, we proceed as follows. First, we estimate the exposure time,  $E_t$ , for each host star and telescope. This is computed to achieve a given signal-to-noise ratio ( $S/N$ ), so that  $S/N = 1/T_{\text{depth}}$  is satisfied. In this case,  $T_{\text{depth}}$  corresponds to the transit depth in percentage, which is taken from the NASA Exoplanet Archive.<sup>2</sup> In addition to the desired  $S/N$ , the calculation of  $E_t$  is carried out considering parameters such as the mean seeing of the site, the brightness of the star, the size of the primary mirror, typical sky brightness of the observatories, the phase of the Moon, and the altitude of the star during the predicted observing windows. Once the exposure times are computed, the derived values are verified and subsequently confirmed by each telescope leader.

Off-transit data have a considerable impact in the determination of the orbital and physical parameters of any transiting system. In the case of ground-based observations, off-transit data are critical in order to remove systematic effects related to changes in airmass, color-dependent extinction, and poor guiding and flatfielding (see, e.g., Southworth et al. 2009; von Essen et al. 2016). To determine the number of data points per transit,  $N$ , hereafter we use the estimated exposure time and the known transit duration,  $T_{\text{dur}}$ , incremented by two hours. This increment accounts for 1 h of off-transit data before and after the transit begins and ends. Then, the number of data points per transit is simply estimated as  $N = (T_{\text{dur}} + 2 \text{ hs}) / (E_t + \text{ROT})$ . Here, ROT corresponds to the readout time of charge-coupled devices used to carry out the observations. To compute the timing precision,  $\sigma_T$ , we use a variant of the formalism provided by Ford & Holman (2007)

$$\sigma_T = \frac{\text{Phot}_p \times T_{\text{dur}}}{N^{1/2} \times T_{\text{depth}}}, \quad (1)$$

where  $\text{Phot}_p$  is the photometric precision in percentage that a given telescope can achieve while observing a 14–15  $K_p$  star. This value was requested to the members of KOINet immediately after they joined the network. Comparing the estimated timing precision with the semi-amplitude of *Kepler* TTVs ( $A_{\text{TTVs}} > 3\sigma_T$ ) yields erroneous results, especially if the TTVs are intrinsically large. For example, an estimated timing precision of 1 h satisfies the above condition for a TTV semi-amplitude of 3 h. However, when ground-based photometry is being analyzed, a timing precision of 1 h would be equal to a non-detection. Therefore, to assign a KOI to a telescope three aspects are simultaneously considered: the transit depth ( $T_{\text{depth}} > \text{Phot}_p$ ), the amplitude of *Kepler* TTVs ( $A_{\text{TTVs}} > 3\sigma_T$ ), and the natural scatter of *Kepler* TTVs ( $2\sigma_{\text{TTVs}} > \sigma_T$ ).

### 2.4.2. Prescription for optimum reference stars

Differential photometry highlights the variability of one star (known as the target star) relative to another (the reference star), which ideally should not vary in time. Thus, the selection of reference stars can limit the precision of photometric data (Young et al. 1991; Howell 2006). The true constancy of reference stars is given by how much they intrinsically vary, subject to the precision that a given optical setup can achieve. Analyzing the flux measurements along the 17 quarters of all the stars within a radius of 5 arcmin relative to KOINet's KOIs, we selected stars that showed a constant flux behavior in time and had a comparable brightness to the given KOI (Howell 2006). In this way, we provide the observer the location of the most photometrically well-behaved reference stars, minimizing the noise budget right from the beginning. Particularly, we have identified between two and five reference stars per field of view, and their location on sky are provided to the observers through KOINet's web interface.

## 2.5. Predictions computed from *Kepler* timings

Using the mid-transit times obtained from *Kepler*'s 17 quarters, we computed TTVs subtracting an averaged (constant) period from them, and classified the KOIs depending on the shape of their TTVs. A full description of the fitting process of *Kepler* transit light curves, the derived values, and their associated errors can be found in Sect. 4.1. Figure 3 shows our four target groups. The simplest case, where the TTVs follow a sinusoidal shape, is shown in the top left panel of the figure. To estimate the predictions for our ground-based follow-up, we fitted to *Kepler* mid-transit times a linear plus a sinusoidal term:

$$TTV(E) = T_0(E = 0) + P_C \times E + A \times \sin[2\pi(\nu E + \phi)]. \quad (2)$$

In this case,  $E$  corresponds to the transit epoch,  $T_0(E = 0)$  to a reference mid-transit time,  $P_C$  to the orbital (constant) period,  $A$  to the semi-amplitude of the TTVs, and  $\nu$  and  $\phi$  respectively to the frequency and phase of the TTVs. The derived predictions are shown in Fig. 3 (green points), while the *Kepler* data is plotted in red and the shape of the predictions, including *Kepler* time, is shown as a continuous black line. Since all *Kepler* mid-times show some scatter, we also estimated errors in the predictions taking this noise into consideration. To increase the chance of transit detection, the magnitudes of the errors in the predictions are provided to the observers, along with a warning. The second TTV scenario is shown in the top right panel of Fig. 3. In this case the available data and the systems themselves allow a more refined dynamical analysis of the TTVs by means of n-body simulations and/or simultaneous transit fitting (see, e.g., Agol et al. 2005; Nesvorný et al. 2013, 2014), from which the predictions are computed. Due to their complexity, a detailed description of the computation of these TTVs is beyond the scope of this paper and will be given individually in future publications. The third case is shown in the bottom left panel of Fig. 3. Here, the number of available *Kepler* transits is not sufficient to carry out a dynamical analysis, and the TTVs do not follow any shape that could give us a hint of when the upcoming transits could occur. Thus, to determine the predictions, we only fit a linear trend to *Kepler* mid-times (i.e., assuming constant period), and use the semi-amplitude of the TTVs as errors for the predictions. The last case exemplifies the need for a ground-based campaign taking place immediately after *Kepler*'s follow-up. This case, displayed in the bottom right panel of Fig. 3, shows an incomplete coverage of the TTV periodicity. From photometry only we cannot assess whether the cause for TTVs is planetary in nature,

<sup>2</sup> <https://exoplanetarchive.ipac.caltech.edu>

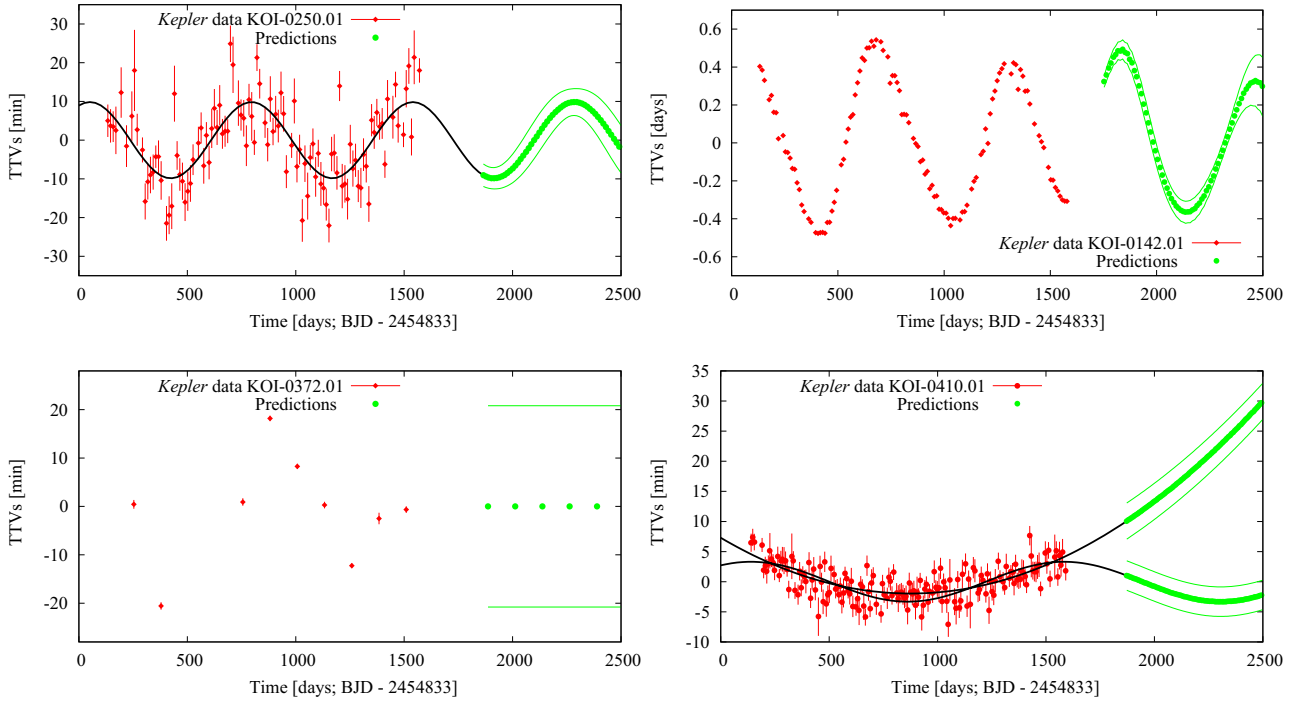


**Fig. 3.** From left to right and top to bottom: sinusoidal, dynamic, chaotic, and parabolic/sinusoidal classification of the TTVs. The TTVs for KOI-0142.01 are given in days, rather than minutes.

is gravitationally bound to the system (e.g., TTVs following a sinusoidal shape), or is due to some completely different scenario, such as TTVs caused by a blended eclipsing binary (TTVs showing a parabolic shape). In this case, we produce two kinds of predictions: sine TTVs, where the predictions are computed as described in Eq. (2), and parabolic TTVs,

$$TTV(E) = T_0(E = 0) + P_C \times E + a \times E^2 + b \times E + c, \quad (3)$$

where  $a$ ,  $b$ , and  $c$  are the fitting coefficients of the parabola. Although these are the two most likely scenarios, the mid-times could also show a different trend. Therefore, until we can disentangle which trend is the one that the system follows, we provide the observers with the two predictions and ask that they observe both of them, and extend the observing time as much as they can.

### 3. Observations and data reduction

#### 3.1. Basic observing setup

In order to ensure that observations are as homogeneous as possible, observers are asked to carry them out in a specific way. To begin with, our observations cover a range of airmass and so are subject to differential extinction effects between the target and comparison stars. To minimize color-dependent systematic effects, observers used intermediate- (Cousins R) or narrow-band (gunn r) filters, depending on the brightness of the target stars and the filter availability. The use of  $R$ -band filters also reduces light curve variations from starspots and limb-darkening effects, and they circumvent the large telluric contamination around the  $I$  band. Furthermore, all observers provide regular calibrations (bias, flatfield frames, and darks, if needed), and are asked to observe with the telescope slightly defocused to minimize the noise in the photometry (Kjeldsen & Frandsen 1992; Southworth et al. 2009). Once the observations are performed, they are collected and reduced in a homogeneous way.

#### 3.2. DIP<sup>2</sup>OL

KOINet data are reduced and analyzed by means of the Differential Photometry Pipelines for Optimum Lightcurves (DIP<sup>2</sup>OL). The pipeline is divided into two parts. The first is based on IRAF's command language. It requires only one reference frame to do aperture photometry. The pipeline carries out normal calibration sequences (bias and dark subtraction and flatfield division, depending on availability) using IRAF task ccdproc. In the particular case of KOINet data, acquired calibrations are always a set of bias and flatfields, taken either at the beginning or end of each observing night. Subject to availability, we correct the science frames of a given observing night only with their corresponding calibrations. In general, we do not take dark frames due to short exposures and cooled, temperature stable CCDs. The reduction continues with cosmic rays rejection (IRAF's cosmicrays) and alignment of the science frames (imalign). Afterwards, reference stars within the field are chosen following specific criteria (for example, that the brightness of the reference stars have to be similar to the brightness of the target star to maximize the S/N of the differential light curves, Howell 2006) and photometric fluxes and errors are measured over the target star and the reference stars as a function of ten different aperture radii and three different sky rings. The annulus and the initial width of the sky ring are set by the user, since they depend on the crowding of the fields. The apertures are non-uniformly distributed between  $0.5 \hat{S}$  and  $5 \times \hat{S}$ , with more density between 1 and  $2 \times \hat{S}$ . Here,  $\hat{S}$  corresponds to the averaged seeing of the images, computed from the full width at half maximum of all the chosen stars in the field. This, in turn, sets a limit to the lowest possible value for the annulus. To perform a posterior detrending of the photometric data, in addition to  $\hat{S}$  the pipeline computes the airmass corresponding to the center of the field of view, the  $(x, y)$  centroid positions of all the measured stars, three sky values originally used to compute the integrated fluxes (one per sky ring), and the integrated counts of the master flat and master dark over the  $(x, y)$  values per frame and per aperture.

The second part of DIP<sup>2</sup>OL is python-based. The routine starts by producing  $N + 1$  light curves from the  $N$  reference fluxes previously computed by IRAF, one with the summed flux of all the  $N$  comparison stars and  $N$  versions with all the reference stars except one. If one of the reference stars is photometrically unstable, the residual light curve corresponding to the unweighted sum of the fluxes of all the reference stars minus this one will show up by giving the lowest standard deviation when compared to the remaining  $N$  residuals. Therefore, this star is removed from the sample. The process of selection and rejection is repeated until the combination of the current available reference stars gives the lowest scatter in the photometry. Since we do not know a priori whether primary transits are actually observed within a given predicted window, residuals are computed by dividing the differential fluxes by a spline function. The pipeline repeats this process through all measured apertures and sky rings, and finds the combination of reference stars, aperture, and sky ring that minimizes the standard deviation of the differential light curves (see, e.g., Ofir et al. 2014). Finally, the code outputs the time in Julian dates shifted to the center of the exposure, the differential fluxes, photometric error bars whose magnitudes have been scaled to match the standard deviation of the residuals,  $(x, y)$  centroid positions, flat counts that were integrated within the final aperture around the given centroids, sky fluxes corresponding to the chosen sky ring, and seeing and airmass values. These quantities will be used in a subsequent step to compute the ground-based detected mid-transit times.

## 4. Data modeling and fitting strategies

### 4.1. Primary transit fitting of Kepler data

One of the key ingredients for the success of our ground-based TTV follow-up is the prior knowledge, with a good degree of accuracy, of the orbital and physical parameters of the systems. To take full advantage of the *Kepler* data in our work, we recomputed the orbital and physical parameters of the 60 KOIs that are included in KOINet's follow-up. A quick view into the Data Validation Reports suggested that the procedures performed over KOIs without TTVs was not optimum for KOIs showing TTVs. Thus, we did not use the transit parameters reported by the NASA Exoplanet Archive. Rather than computing time-expensive photo-dynamical solutions over the 60 KOIs (see, e.g., Barros et al. 2015), to minimize the impact of the TTVs in the computation of the transit parameters we fitted two consecutive transit light curves simultaneously with a Mandel & Agol (2002) transit model, making use of their occultquad routine.<sup>3</sup> From the transit light curve we can determine the following parameters: the orbital period,  $P$ ; the mid-transit time,  $T_0$ ; the planet-to-star radius ratio,  $R_p/R_s$ ; the semi-major axis in stellar radius,  $a/R_s$ ; and the orbital inclination,  $i$ , in degrees. For all the KOIs we assumed circular orbits. Furthermore, we assumed a quadratic limb-darkening law with fixed limb-darkening coefficients,  $u_1$  and  $u_2$ . For the *Kepler* data we used the limb-darkening values specified in Claret et al. (2013), choosing as fundamental stellar parameters the effective temperature, metallicity, and surface gravity, from the values listed in the NASA Exoplanet Archive. Simultaneously to the transit model we fitted a time-dependent second-order polynomial to account for out-of-transit variability. To determine reliable errors for the fitted parameters, we explored the parameter space by sampling from the posterior-probability distribution using a Markov chain Monte

<sup>3</sup> <http://www.astro.washington.edu/users/agol>

Carlo (MCMC) approach. Our MCMC calculations make extensive use of routines of PyAstronomy,<sup>4</sup> a collection of Python built-in functions that provide an interface for fitting and sampling algorithms implemented in the PyMC (Patil et al. 2010) and SciPy (Jones et al. 2001) packages. We refer the reader to their detailed online documentation.<sup>5</sup> For the computation of the best-fit parameters we iterated 80 000 times per consecutive transits, and conservatively discarded the first 20%. As starting values for the parameters we used those specified in the NASA Exoplanet Archive. To set reasonable limits for the MCMC uniform probability distributions, we chose  $R_p/R_s \pm 0.1$ ,  $T_0 \pm T_{\text{Dur}}/3$ , and a considerable fraction of the orbital period, depending on the amplitude of *Kepler* TTVs. These values are relative to the values determined by the *Kepler* team. The semi-major axis and the inclination are correlated through the impact parameter,  $a/R_s \cos(i)$ . Thus, rather than using uniform distributions for these parameters, we used Gaussian priors with the mean and the standard deviation equal to the values found in the NASA Exoplanet Archive and three times their errors, respectively. To compute the transit parameters, we analyzed *Kepler* long-cadence transit data. To minimize the impact of the sampling rate on the determination of the transit parameters (see, e.g., Kipping 2010), during each instance of primary transit fitting we used a transit model calculated from a finer timescale and then averaged over the *Kepler* timing points. In particular, 30 equally spaced points were calculated and averaged to one data point. The modeling of all consecutive transits results in a parameter distribution for the semi-major axis, the inclination, the orbital period and the planet-to-star radius ratio. We used their mean values and standard deviations to limit the ground-based data fitting (Sect. 4.2). All the orbital and physical parameters computed for the 60 KOIs are summarized in the right part of Table 2. Errors are at the  $1-\sigma$  level. It is worth mentioning that the transit parameters presented in the table provide us with an excellent transit template to be used to fit ground-based data. It is not our intention to improve any of the parameters by means of this simple analysis. A more detailed approach, such as photo-dynamical fitting might be required (see, e.g., Barros et al. 2015), especially with large-amplitude TTVs such as Kepler-9 (KOI-0377.01/02, Holman et al. 2010; Ofir et al. 2014). As an example, Fig. 4 shows how the transit parameters change as a function of time, evidencing their mutual correlations and the rate and amplitude at which they change. As expected, for the values in the figure the Pearson's correlation coefficient between the semi-major axis and the inclination is  $r_{a/R_s, i} = 0.96$ , while these two reveal a strong anti-correlation with the planet-to-star radius ratio ( $r_{R_p/R_s, i} = -0.91$ , and  $r_{R_p/R_s, a/R_s} = -0.93$ ).

### 4.2. Primary transit fitting and detrending of ground-based data

Once DIP<sup>2</sup>OL returns the photometric light curve and the associated detrending quantities, the computation of ground-based TTVs begins. First, we convert the time-axis, originally given in Julian dates, to Barycentric Julian dates using the Eastman et al. (2010) web tool.<sup>1</sup> To do so, we make use of the celestial coordinates of the star, the geographic coordinates of the site, and the height above sea level. Throughout this work, our model comprises primary transit times, a detrending

<sup>4</sup> <http://www.hs.uni-hamburg.de/DE/Ins/Per/Czesla/PyA/PyA/index.html>

<sup>5</sup> <http://pymc-devs.github.io/pymc/>

<sup>1</sup> <http://astroutils.astronomy.ohio-state.edu/time/utc2bjd.html>

**Table 2.** Basic parameters from the KOIs presented in this work.

KOI Nr.	$\alpha$ (J2000) ( $^{\circ}$ )	$\delta$ (J2000) ( $^{\circ}$ )	$K_p$	$a/R_S$	$i$ ( $^{\circ}$ )	$R_p/R_S$	Per (days)	O14–15
0094.01	297.333069	41.891121	12.205	$27.27 \pm 0.03$	$89.997 \pm 0.001$	$0.0691 \pm 0.0001$	$22.34285 \pm 0.00078$	–
0094.03	297.333069	41.891121	12.205	$50.5 \pm 0.2$	$89.93 \pm 0.01$	$0.0411 \pm 0.0003$	$54.3198 \pm 0.0018$	–
0142.01	291.148071	40.669399	13.113	$16.9 \pm 0.9$	$87.4 \pm 0.3$	$0.038 \pm 0.001$	$10.947 \pm 0.036$	6
0250.01	284.940979	46.566540	15.473	$32 \pm 2$	$89.29 \pm 0.07$	$0.051 \pm 0.002$	$12.2827 \pm 0.0044$	2
0250.02	284.940979	46.566540	15.473	$54 \pm 6$	$89.3 \pm 0.2$	$0.047 \pm 0.005$	$17.2509 \pm 0.0097$	1
0315.01	297.271881	43.333309	12.968	$59 \pm 5$	$89.6 \pm 0.2$	$0.029 \pm 0.001$	$35.5812 \pm 0.0087$	4
0318.01	288.153992	44.068821	12.211	$29.1 \pm 0.2$	$89.9 \pm 0.2$	$0.033 \pm 0.003$	$38.5846 \pm 0.0049$	–
0345.01	286.524811	48.683601	13.340	$45 \pm 3$	$89.4 \pm 0.2$	$0.0335 \pm 0.0009$	$29.8851 \pm 0.0031$	–
0351.01	284.433502	49.305161	13.804	$186.2 \pm 0.1$	$89.970 \pm 0.001$	$0.0852 \pm 0.0001$	$331.616 \pm 0.025$	1
0351.02	284.433502	49.305161	13.804	$141 \pm 1$	$90.001 \pm 0.001$	$0.0601 \pm 0.0008$	$210.79 \pm 0.41$	1
0372.01	299.122437	41.866760	12.391	$112 \pm 1$	$89.98 \pm 0.08$	$0.0816 \pm 0.0009$	$125.6287 \pm 0.0073$	–
0377.01	285.573975	38.400902	13.803	$33 \pm 2$	$89.1 \pm 0.2$	$0.078 \pm 0.001$	$19.245 \pm 0.023$	12
0377.02	285.573975	38.400902	13.803	$55 \pm 6$	$89.3 \pm 0.2$	$0.076 \pm 0.003$	$38.95 \pm 0.11$	2
0410.01	292.248016	40.696049	14.454	$33 \pm 6$	$89.0 \pm 0.9$	$0.065 \pm 0.007$	$7.2165 \pm 0.0018$	6
0448.02	297.070160	40.868790	14.902	$45 \pm 10$	$88.9 \pm 0.6$	$0.05 \pm 0.01$	$43.587 \pm 0.022$	9
0456.01	287.773560	42.869282	14.619	$20.4 \pm 0.7$	$88.35 \pm 0.07$	$0.034 \pm 0.001$	$13.699 \pm 0.012$	3
0464.01	293.747101	45.107220	14.361	$75.0 \pm 0.3$	$89.95 \pm 0.01$	$0.0677 \pm 0.0008$	$58.3619 \pm 0.0023$	–
0523.01	286.047119	45.053211	15.000	$45 \pm 5$	$88.9 \pm 0.2$	$0.063 \pm 0.003$	$49.4112 \pm 0.0082$	1
0525.01	300.907776	45.457870	14.539	$20 \pm 2$	$87.3 \pm 0.3$	$0.05 \pm 0.01$	$11.5300 \pm 0.0093$	4
0528.02	287.101105	46.896481	14.598	$102 \pm 9$	$89.6 \pm 0.1$	$0.031 \pm 0.002$	$96.676 \pm 0.010$	–
0620.01	296.479767	49.937679	14.669	$62.7 \pm 0.4$	$89.90 \pm 0.02$	$0.074 \pm 0.001$	$45.1552 \pm 0.0028$	1
0620.02	296.479767	49.937679	14.669	$127.2 \pm 0.6$	$89.98 \pm 0.01$	$0.1017 \pm 0.0009$	$130.1783 \pm 0.0058$	–
0638.01	295.559418	40.236271	13.595	$36.1 \pm 0.3$	$89.65 \pm 0.06$	$0.032 \pm 0.001$	$23.6415 \pm 0.0069$	2
0738.01	298.348328	47.491230	15.282	$27 \pm 4$	$88.79 \pm 0.07$	$0.037 \pm 0.003$	$10.338 \pm 0.015$	4
0738.02	298.348328	47.491230	15.282	$24 \pm 2$	$88.33 \pm 0.05$	$0.034 \pm 0.005$	$13.286 \pm 0.019$	–
0757.02	286.999481	48.375790	15.841	$68 \pm 2$	$89.73 \pm 0.07$	$0.046 \pm 0.003$	$41.196 \pm 0.011$	–
0759.01	285.718536	48.504849	15.082	$37 \pm 4$	$88.8 \pm 0.3$	$0.044 \pm 0.003$	$32.628 \pm 0.017$	3
0760.01	292.167053	48.727589	15.263	$12.2 \pm 0.4$	$86.0 \pm 0.2$	$0.106 \pm 0.003$	$4.9592 \pm 0.0012$	7
0806.01	285.283630	38.947281	15.403	$124 \pm 7$	$89.84 \pm 0.09$	$0.099 \pm 0.001$	$143.200 \pm 0.059$	3
0806.02	285.283630	38.947281	15.403	$75 \pm 3$	$89.9 \pm 0.1$	$0.136 \pm 0.003$	$60.3258 \pm 0.0062$	4
0829.03	290.461761	40.562462	15.386	$37 \pm 3$	$88.7 \pm 0.1$	$0.033 \pm 0.003$	$38.557 \pm 0.024$	–
0841.01	292.236755	41.085880	15.855	$31.3 \pm 0.9$	$89.21 \pm 0.07$	$0.054 \pm 0.004$	$15.334 \pm 0.011$	1
0841.02	292.236755	41.085880	15.855	$39 \pm 5$	$88.9 \pm 0.3$	$0.08 \pm 0.01$	$31.3304 \pm 0.0077$	3
0854.01	289.508484	41.812119	15.849	$89 \pm 5$	$89.75 \pm 0.05$	$0.041 \pm 0.002$	$56.052 \pm 0.021$	1
0869.02	291.638977	42.436321	15.599	$57 \pm 2$	$89.64 \pm 0.08$	$0.037 \pm 0.001$	$36.277 \pm 0.027$	1
0880.01	292.873383	42.966141	15.158	$36 \pm 5$	$88.7 \pm 0.4$	$0.045 \pm 0.006$	$26.4435 \pm 0.0097$	1
0880.02	292.873383	42.966141	15.158	$51 \pm 6$	$89.3 \pm 0.2$	$0.061 \pm 0.002$	$51.537 \pm 0.021$	7
0886.01	294.773926	43.056301	15.847	$8.9 \pm 0.4$	$83.7 \pm 0.1$	$0.07 \pm 0.02$	$8.009 \pm 0.015$	1
0902.01	287.852386	43.897991	15.754	$85 \pm 7$	$89.6 \pm 0.1$	$0.089 \pm 0.002$	$83.927 \pm 0.016$	7
0918.01	283.977509	44.811562	15.011	$51.6 \pm 0.2$	$89.93 \pm 0.02$	$0.116 \pm 0.002$	$39.6432 \pm 0.0016$	3
0935.01	294.023010	45.853081	15.237	$30.9 \pm 0.5$	$89.5 \pm 0.1$	$0.042 \pm 0.001$	$20.860 \pm 0.011$	1
0935.02	294.023010	45.853081	15.237	$40 \pm 3$	$89.0 \pm 0.2$	$0.042 \pm 0.002$	$42.6334 \pm 0.0081$	–
0935.03	294.023010	45.853081	15.237	$52 \pm 7$	$89.1 \pm 0.3$	$0.034 \pm 0.002$	$87.647 \pm 0.019$	–
0984.01	291.048798	36.839882	11.631	$20.6 \pm 0.7$	$88.8 \pm 0.1$	$0.030 \pm 0.001$	$4.2888 \pm 0.0031$	8
1199.01	293.743927	38.939281	14.887	$72 \pm 2$	$89.77 \pm 0.08$	$0.030 \pm 0.002$	$53.526 \pm 0.021$	–
1271.01	294.265503	44.794300	13.632	$105 \pm 3$	$89.64 \pm 0.02$	$0.0693 \pm 0.0005$	$161.98 \pm 0.16$	4
1353.01	297.465332	42.882839	13.956	$112 \pm 3$	$89.85 \pm 0.07$	$0.105 \pm 0.001$	$125.8648 \pm 0.0029$	7
1366.01	286.358063	42.406509	15.368	$29 \pm 1$	$88.9 \pm 0.1$	$0.031 \pm 0.003$	$19.256 \pm 0.019$	1
1366.02	286.358063	42.406509	15.368	$47 \pm 12$	$88.7 \pm 0.5$	$0.05 \pm 0.02$	$54.156 \pm 0.021$	–
1426.01	283.209167	48.777641	14.232	$48.3 \pm 0.6$	$89.67 \pm 0.09$	$0.029 \pm 0.001$	$38.868 \pm 0.011$	–
1426.02	283.209167	48.777641	14.232	$93 \pm 11$	$89.6 \pm 0.2$	$0.065 \pm 0.002$	$74.927 \pm 0.011$	1
1426.03	283.209167	48.777641	14.232	$131 \pm 8$	$89.56 \pm 0.05$	$0.12 \pm 0.03$	$150.025 \pm 0.013$	–
1429.01	292.351501	48.511082	15.531	$114 \pm 21$	$89.6 \pm 0.2$	$0.051 \pm 0.003$	$205.914 \pm 0.021$	–
1474.01	295.417877	51.184761	13.005	$50.4 \pm 0.7$	$88.69 \pm 0.05$	$0.25 \pm 0.03$	$69.721 \pm 0.032$	2
1573.01	296.846161	40.138611	14.373	$59.4 \pm 0.9$	$89.80 \pm 0.06$	$0.045 \pm 0.001$	$24.8093 \pm 0.0058$	6
1574.01	297.916870	46.965130	14.600	$60 \pm 10$	$89.3 \pm 0.2$	$0.067 \pm 0.003$	$114.7356 \pm 0.0079$	–
1574.02	297.916870	46.965130	14.600	$48 \pm 7$	$88.9 \pm 0.2$	$0.036 \pm 0.001$	$191.29 \pm 0.17$	–
1873.01	295.809296	40.008511	15.674	$63.9 \pm 0.4$	$89.90 \pm 0.02$	$0.045 \pm 0.002$	$71.3106 \pm 0.0087$	–
2672.01	296.132812	48.977402	11.921	$80 \pm 12$	$89.5 \pm 0.2$	$0.051 \pm 0.003$	$88.508 \pm 0.013$	–
2672.02	296.132812	48.977402	11.921	$72.2 \pm 0.3$	$89.92 \pm 0.01$	$0.0303 \pm 0.0009$	$42.9933 \pm 0.0042$	–

From left to right: KOI number; right ascension,  $\alpha$ , and the declination,  $\delta$ , in degrees (J2000.0); *Kepler* magnitude,  $K_p$ . The values are from the NASA Exoplanet Archive. Semi-major axis in stellar radii,  $a/R_S$ ; inclination in degrees,  $i$ ; planet-to-star radius ratio,  $R_p/R_S$ ; orbital period in days, Per; and number of observations collected during 2014 and 2015.

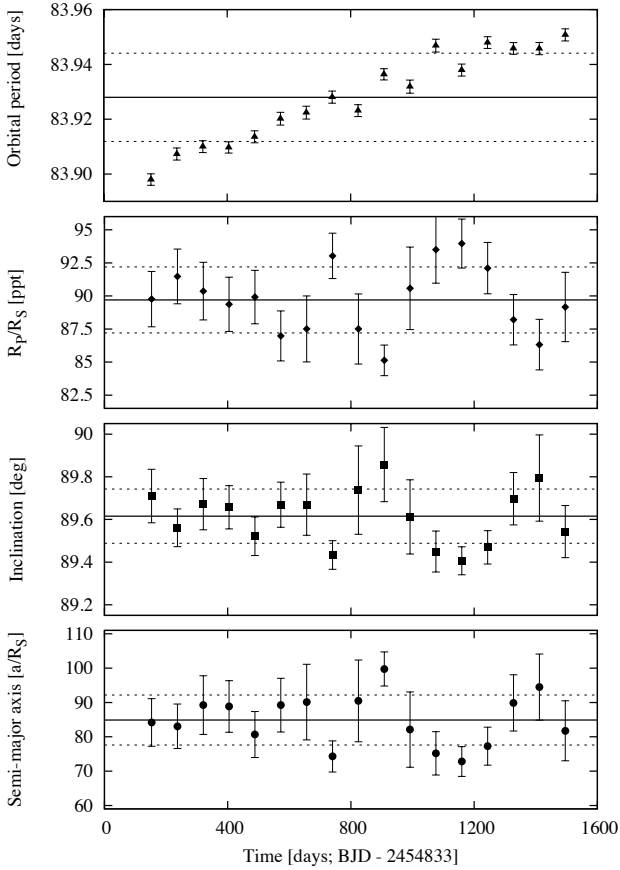


**Fig. 4.** Time-dependent change in the transit parameters of KOI-0902.01. *From top to bottom*: orbital period in days (triangles); planet-to-star radius ratio,  $R_p/R_s$  (diamonds); orbital inclination (squares), and semi-major axis in stellar radii,  $a/R_s$ . Horizontal continuous and dashed lines show mean and standard deviations of the system parameters, respectively. Individual errors are given at the 1- $\sigma$  level.

component. Thus, to compute TTVs we carry out a more refined detrending of the light curves rather than just a time-dependent polynomial. For the detrending model we consider a linear combination of seeing, airmass,  $(x, y)$  centroid positions of the target and of the reference stars, integrated counts over the selected photometric aperture, and the  $(x, y)$  centroid positions of the master flat field and the master dark frames, when available, and integrated sky counts for the selected sky ring (see, e.g., Kundurthy et al. 2013; Becker et al. 2013 for a similar approach in the detrending strategy). Due to the nature of the data the exact time at which the mid-transits will occur are in principle unknown, or known but with a given certainty. Some photometric observations could actually have been taken outside the primary transit occurrence. As a consequence, we have to be extremely careful not to overfit our data. In order to choose a sufficiently large number of fitting parameters we take into consideration the joint minimization of four statistical indicators: the reduced- $\chi^2$  statistic,  $\chi^2_{red}$ ; the Bayesian Information Criterion,  $BIC = \chi^2 + k \ln(Q)$ ; the standard deviation of the residual light curves enlarged by the number of fitting parameters,  $\sigma_{res} \times k$ ; and the Cash statistic (Cash 1979),  $Cash = 2 \sum_{i=1}^Q M_i - D_i * \ln(M_i)$ , being  $M$  the model and  $D$  the data. For the BIC,  $k$  is the number of fitting parameters, and  $\chi^2$  is computed from the residuals obtained by subtracting the best-fit model from the synthetic data. For the BIC and Cash,  $Q$  is the number of data points per light curve. The full detrending model,

$DM$ , has the following expression:

$$DM(t) = c_0 + c_1 \times \hat{\chi} + c_2 \times \hat{S} + \sum_{i=1}^{N+1} bg_i \times BG_i + fc_i \times FC_i + dk_i \times DK_i + x_i \times X_i + y_i \times Y_i \quad (4)$$

Here,  $N + 1$  denotes the total number of target and reference stars;  $\hat{S}$  and  $\hat{\chi}$  correspond to seeing and airmass, respectively;  $X_i$  and  $Y_i$  are the  $(x, y)$  centroid positions;  $FC_i$  and  $DK_i$  are the integrated flat and dark counts in the chosen aperture, respectively; and  $BG_i$  correspond to the background counts. The coefficients of the detrending model are  $c_0, c_1, c_2$ ;  $bg_i, fc_i, dk_i$ ; and  $x_i, y_i$ , with  $i = 1, N + 1$ . Using a linear combination of these components simplifies the computation of the detrending coefficients that accompany them by means of simple inversion techniques. Rather than using the full detrending model to clean the data of systematics and potentially overfit the data, we evaluate the submodels (i.e., a linear combination of some of the detrending components). Typical detrending functions would have the following expression:

$$DM_0 = c_0,$$

$$DM_1 = c_0 + c_1 \hat{\chi},$$

$$DM_2 = c_0 + c_1 \hat{\chi} + c_2 \hat{S},$$

$$DM_3 = c_0 + c_2 \hat{S},$$

$$DM_4 = c_0 + \sum_{i=1}^{N+1} bg_i \times BG_i,$$

$$DM_5 = c_0 + c_1 \hat{\chi} + \sum_{i=1}^{N+1} bg_i \times BG_i,$$

...

$$DM_{14} = c_0 + c_1 \hat{\chi} + c_2 \hat{S} + \sum_{i=1}^{N+1} bg_i \times BG_i + x_i \times X_i + y_i \times Y_i.$$

... (5)

In the equation,  $N$  corresponds either to the total number of reference stars or to 0. Indeed, we evaluate Eq. (5) taking into account the quantities associated with all the reference stars selected to construct the differential light curve and the target, but also the target alone ( $N+1$  and 1, but not any combination in between). DIP<sup>2</sup>OL considers a total of 88 submodels, depending on the availability of calibrations. Usually, the noise in the data is correlated with airmass,  $(x, y)$  centroid positions, and integrated flat counts, while the dependency with seeing strongly depends on the photometric quality and stability of the particular night. Therefore, these 88 submodels are constructed solely from how we think the systematics impact the data. Although all possible combinations should be tested, this is computationally expensive, especially considering that a differential light curve can be constructed averaging 20–30 reference stars (i.e.,  $N = 20$ –30).

To determine the detrending submodel best matching the residual noise in the data, we first create an array of trial  $T_0$  values around the predicted mid-transit time, covering the  $\pm T_{dur}$  space and respecting the cadence of the observations. For each of these trial  $T_0$ 's and each one of the submodels considered in our modeling, we compute the previously mentioned four

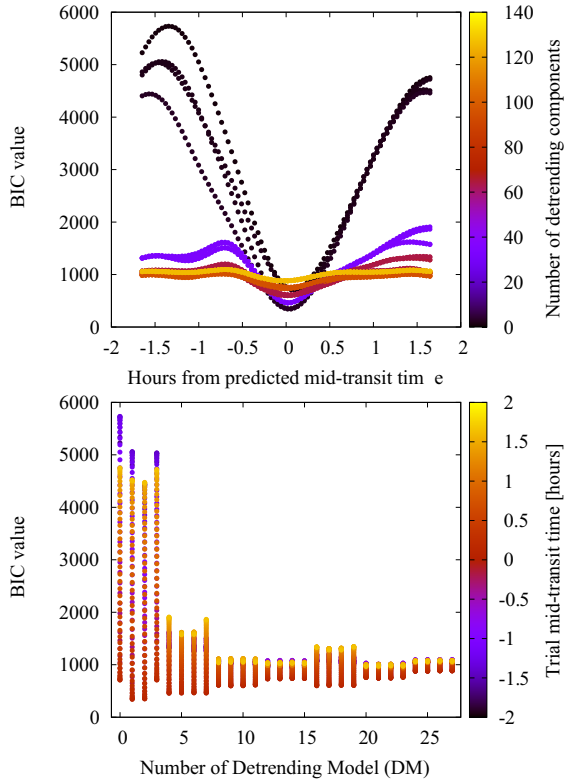


**Fig. 5.** *Top:* BIC values as a function of trial mid-transit times. Color-coded are the number of detrending components for each of the detrending models (submodels). Darker colors correspond to a smaller number of detrending components. *Bottom:* same BIC values, but now as a function of the detrending model, DM. Numbers on the abscissa are in agreement with the labels on Eq. (5). Color-coded are the trial  $T_0$ 's. According to the color scale, red points correspond to  $T_0 = 0$ .

statistics. This takes care of the uncertainty in the knowledge of the mid-transit times, since typical errors in the predictions of transits with large TTVs can increase up to 40–50 minutes, in some cases even more. Indeed, dealing with incomplete, shallow transit light curves with large TTVs imposes some extra nursing in our detrending strategy. On the one hand, the choice of detrending model should not have a significant impact on the determination of the mid-transit time. Thus, if a given trial  $T_0$  is close to the true mid-transit time, then the choice of detrending model should have no significant impact on the minimization of the statistics. In other words, around this  $T_0$  all the submodels should minimize the four statistics. To illustrate this, we analyzed in detail the transit photometry of KOI-0760.01 taken with NOT 2.5 m. Figure 5, top, shows how the BIC changes as a function of the trial  $T_0$ , for all the possible submodels (28 in this case, since dark frames were unavailable). The number of detrending components are color-coded. As previously mentioned, this serves to show how the mid-transit time is globally independent of the choice of detrending components, and shows how the BIC on average is always minimized around the same  $T_0$ . On the other hand, several detrending models could do a proper job of finding an adequate  $T_0$ , but perhaps at the cost of an unnecessarily large number of detrending components. To illustrate this, Fig. 5, bottom, shows the dependency between the BIC and the detrending models. For a better comparison between the figure and our detrending models, the numbers on the abscissa are in concordance with the indices in Eq. (5). The values for the trial  $T_0$ 's are color-coded. The figure reveals how all the detrending models minimize the BIC around the same  $T_0$ , imposing

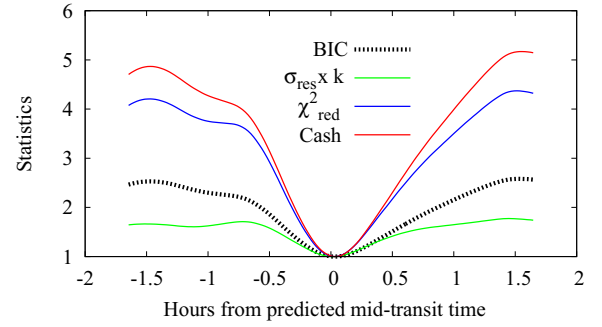


**Fig. 6.** Four statistics used to assess the number of detrending components and the starting mid-transit time, obtained by analyzing the KOI-0760 data. Their values have been normalized and scaled to allow for visual comparison. The thick dashed black line corresponds to the time-averaged BIC statistics, as shown in the top panel of Fig. 5.

the need for extra care in identifying the number of detrending components. In particular, our code uses the minimization of the time-averaged statistics (i.e., the four statistics averaged for each of the trial  $T_0$ 's) to determine the starting value of the mid-transit time that will be used in our posterior transit fitting (see Fig. 6). This is a more robust approach than simply computing the absolute minimum value of the statistics. With this mid-transit time fixed we recompute the transit model and reiterate over all the detrending models to finally choose the one that minimizes the averaged statistics.

For the transit fitting instance we use a quadratic limb-darkening law with quadratic limb-darkening values computed as described in von Essen et al. (2013), for the filter band matching the one used during the observations and for the stellar fundamental parameters closely matching the ones of the KOIs. Rather than considering the orbital period, the inclination, the semi-major axis and the planet-to-star radius ratio as fixed parameters to the values given by the NASA Exoplanet Archive or the values derived in Table 2, we use a Gaussian probability distribution with mean and standard deviation matching the values obtained in Sect. 4.1, and we fit all of them simultaneously to the detrending model and the mid-transit time. The inclination, semi-major axis, and planet-to-star radius ratio are fitted only if the light curves show complete transit coverage. If not, we consider them as fixed to the values reported in Table 2, and we fit only the mid-transit time. At each MCMC step the transit parameters change. Therefore, for each iteration we compute the detrending coefficients with the previously mentioned inversion technique. To fit KOINet's ground-based data we produce  $5 \times 10^6$  repetitions of the MCMC chains, we discard the first 20%, and we compute the mean and standard deviation ( $1-\sigma$ ) of the posterior distributions of the parameters as best-fit values and uncertainties, respectively. To check for the convergence of the chains, we divide the remaining 80% in four, and we compute mean and standard deviations of the priors within each 20%. We consider that the chains converged if all the values are consistent within  $1-\sigma$  errors. Finally, we visually inspect the posterior distributions and their correlations.

To provide reliable error bars on the timing measurements we evaluate to what extent our photometric data are affected by correlated noise. To this end, following Carter & Winn (2009) we compute residual light curves by dividing our photometric data by the best-fit transit and detrending models. From the residuals, we compute the  $\beta$  factors as specified in von Essen et al. (2013). Here, we divide each residual light curve into  $M$  bins of  $N$  averaged data points. If the data are free of correlated

**Table 3.** Most relevant parameters obtained from our observations.

Date yyyy.mm.dd	Telescope	Name	$\sigma_{res}$ (ppt)	$N$	CAD (sec)	$T_{tot}$ (hours)	$\chi_{min,max}$	TC	TTVs $\pm 1-\sigma$ BJD <sub>TDB</sub>
2014.06.24	IAC 0.8 m	KOI-0902.01	1.8	114	210	6.67	1.03,1.63	–BEO	2456832.43925 $\pm$ 0.0063
2014.08.28	ARC 3.5 m	KOI-0525.01	0.7	135	60	2.26	1.02,1.06	OIBE-	2456897.71506 $\pm$ 0.0045
2014.10.03	NOT 2.5 m	KOI-0760.01	1.4	302	59	5.00	1.07,2.50	OIBEO	2456934.43353 $\pm$ 0.0010
2014.10.12	NOT 2.5 m	KOI-0410.01	1.0	178	81	4.01	1.06,2.29	OIBEO	2456943.41142 $\pm$ 0.0018
2014.11.03	YO 2.4 m	KOI-0410.01	1.4	128	110	3.91	1.10,2.78	OIBEO	2456965.06535 $\pm$ 0.0020
2015.07.06	CAHA 2.2 m	KOI-0410.01	3.7	670	41	7.75	1.00,1.50	OIBEO	2457210.43420 $\pm$ 0.0031
2015.07.06	NOT 2.5 m	KOI-0410.01	0.8	142	95	3.77	1.02,1.51	–IBEO	2457210.43652 $\pm$ 0.0022

**Notes.** From left to right: date corresponding to the beginning of the local night in years, months, and days (yyyy.mm.dd); telescope performing the observations; name of the observed KOI; standard deviation of the residual light curves in parts per thousand (ppt),  $\sigma_{res}$ ; number of data points per light curve,  $N$ ; average cadence in seconds, CAD; total observing time in hours,  $T_{tot}$ ; airmass range,  $\chi_{min,max}$ , showing minimum and maximum values; transit coverage, TC; and derived mid-transit times, in BJD<sub>TDB</sub>. Acronyms for the telescopes are as specified in Sect. 2.3. The letter code specifying the transit coverage during each observation is as follows: O: out of transit, before ingress; I: ingress; B: flat bottom; E: egress; O: out of transit, after egress.

noise, then the noise within the residual light curves should follow the expectation of independent random numbers:

$$\hat{\sigma}_N = \sigma_1 N^{-1/2} [M/(M-1)]^{1/2}. \quad (6)$$

Here,  $\sigma_1$  corresponds to the scatter of the unbinned residuals, and  $\sigma_N$  to the variance of the binned data:

$$\sigma_N = \sqrt{\frac{1}{M} \sum_{i=1}^M (\langle \hat{\mu}_i \rangle - \hat{\mu}_i)^2}. \quad (7)$$

In the equation, the mean value of the residuals per bin is given by  $\hat{\mu}_i$ , and  $\langle \hat{\mu}_i \rangle$  is the mean value of the means. In the presence of correlated noise,  $\sigma_N$  should differ by the factor  $\beta_N$  from  $\hat{\sigma}_N$ . Therefore, we compute  $\beta$  by averaging the  $\beta_N$ 's obtained over time bins close to the duration of ingress, which in turn is computed from the previously determined best-fit transit parameters. In particular, we consider time bins as large as 0.8, 0.9, 1, 1.1, and 1.2 times the duration of ingress. If  $\beta$  is larger than 1, we enlarge the photometric error bars by this value, and we carry out the MCMC fitting in the exact same fashion as previously explained. We conclude by visually inspecting the data, the detrending model, and the best-fit transit model.

## 5. KOINet's achieved milestones

### 5.1. Photometric data presented in this work

Here we present seven new primary transit observations of KOI-0760.01, KOI-0410.01, KOI-0525.01, and KOI-0902.01. These were taken between May 2014 and July 2015. Table 3 shows the basic photometric characteristics of the data, such as the photometric precision, the cadence and number of data points per light curve, the transit coverage, and the dates at which the KOIs were observed. The last column of Table 3 shows their corresponding mid-transit times, along with  $1-\sigma$  uncertainties. The KOIs presented in this work were chosen to exemplify the need for a network such as KOINet, as described in the following sections.

We would like to emphasize that the purpose of this paper is to show the potential of KOINet. Therefore, we present the TTV observations, together with preliminary models. For individual cases (e.g., KOI-0410.01) a more in-depth analysis is also given.

Most of the KOIs that are members of the KOINet follow-up are in wide orbits. In particular, the average orbital period of these KOIs is around 65 days, while the largest orbit corresponds to 335 days. As a consequence, most of the transits last several hours, with an average value of about  $6 \pm 3$  h. Thus, it is challenging to cover the full transit from the ground. Normally, incomplete transit coverage has a large impact on the determination of the mid-transit times (see, e.g., Winn et al. 2008; Gibson et al. 2009). However, in our case this is alleviated by the prior knowledge of the orbital parameters given by *Kepler* photometry. While long-cadence *Kepler* data were obtained averaging images of 30 min each, the collected ground-based observations have a cadence between a few seconds and a few minutes. Although our Earth's atmosphere and typical ground-based instrumental imperfections considerably decrease the photometric precision when compared to the *Kepler* data, we gain in sampling rate and thus in timing precision, given the prior knowledge of the transit parameters.

### 5.2. Timing precision: KOI-0760.01

Figure 10a, shows a primary transit of KOI-0760.01 and its corresponding TTVs. The target is a Neptune-sized planet candidate in a  $\sim 5$  day orbit, showing TTVs of small amplitude ( $\sim 140$  s). The TTV period is around 3.5 yr and, as a consequence, has been roughly covered by the *Kepler* data. The TTVs also show a scatter of  $\sim 2$  min. To include a KOI into KOINet's follow-up list, it has to fulfill specific conditions. One of them is to present TTVs equal to or larger than about 2 min. KOI-0760.01 is close to the lower end of this limit. Compared with *Kepler* averaged errors in the mid-transit times ( $\sim 80$  s) ground-based data collected by KOINet delivered a timing precision of the same quality. The left panel of Fig. 10a, shows a detrended transit light curve (in green), the best-fit model (black continuous line), and the raw data and detrended model (blue points and black continuous line, respectively). For a better visualization, these were arbitrarily shifted. The figure on the right shows *Kepler* and ground-based TTVs (red diamonds). The red and green shaded areas indicate *Kepler* coverage and the ground-based, 2014 observing season, respectively.

### 5.3. Photometric precision: KOI-0525.01

Another strong limit set by the nature of ground-based observations is given by the transit depth. For *Kepler* targets with TTVs,

this is aggravated by the faintness of the stars, the length of the transits, and the uncertainty of the transit occurrence. Before starting the observing seasons we set an ambitious lower limit in the transit depth of  $\sim 1$  ppt, with the final cut given by the TTV amplitude and the transit duration. To maximize the transit detection, we assigned these transits to the largest telescopes. One successful example of our observing strategy is given by KOI-0525.01. The KOI is labeled as an exoplanet candidate, and in addition to a small transit depth ( $\sim 1$  ppt), it has an orbital period of  $\sim 11.5$  days, and a transit duration of  $\sim 2.25$  h, facilitating observations of complete transits from the ground. The TTV periodicity shown by the *Kepler* data is longer than four years, so our observations will help to set constraints on the nature of the KOI. Figure 10b, shows the ground-based light curve obtained with the ARC 3.5 m telescope. We detected the transit and a turnover in the TTVs of KOI-0525.01, shown on the right side of Fig. 10b. With the addition of the holographic diffruser on the new ARCTIC imager on the ARC 3.5 m telescope at Apache Point Observatory, we may be able to achieve even higher photometric precision in future observations (Stefansson et al. 2017).

#### 5.4. Relevance for ground-based follow-ups: KOI-0902.01

When the TTV periodicity is not fully sampled, the quickly increasing separation between the two most likely scenarios (sinusoidal and parabolic predictions) can prevent us from finding future transits of these KOIs. For some KOIs (e.g., KOI-0410.01; see next section) the difference between these two extreme scenarios is on the order of 2 min and will be well contained below a few hours in the near future. However, for some other KOIs the current difference is larger than the duration of an observing night. Therefore, if follow-up campaigns are not carried out in time, it will be extremely expensive to detect the transits of these planet candidates again. A clear example of this is given by KOI-0902.01. The exoplanet candidate is in an  $\sim 84$ -day orbit, and the transit duration is of  $\sim 6.7$  h, making the full observation of a single transit quite challenging from only one observing site. Figure 10c, shows one of the transits observed by the IAC 0.8 m telescope. The transit ( $\Delta F \sim 1\%$ ) was clearly detected by KOINet. In the right panel, the TTVs of the *Kepler* data plus the ground-based detected mid-time can be seen.

#### 5.5. Turnover of TTVs: KOI-0410.01

In the NASA Exoplanet Archive, more specifically within the Data Validation Reports (DV), KOI-0410.01 is identified as a false positive. Most of the evidence in favor of this status is based upon the V-shape of its transits. The flux drops take place every  $\sim 7.2$  days, and the transit depth is about 5 ppt. During 2014 and 2015 we observed four transits of KOI-0410.01. The characteristics of the data are presented in Table 3. The combination of *Kepler* and ground-based TTVs reveal a turnover in their mid-times (see Fig. 10d). This, together with the assigned status, motivates a more detailed study to shed some light onto the nature of the system.

To begin with, in the DV report a source of 18.4 *Kepler* magnitudes has been detected, approximately nine arcseconds away from the nominal position of KOI-0410. Therefore, it is possible that a background eclipsing binary could be causing the observed flux drops there. For spatially resolved ground-based observations, 9 arcseconds corresponds to several dozens of pixels. To identify the source, we combined all the observations of our best (sharpest) night. Once the mentioned source was

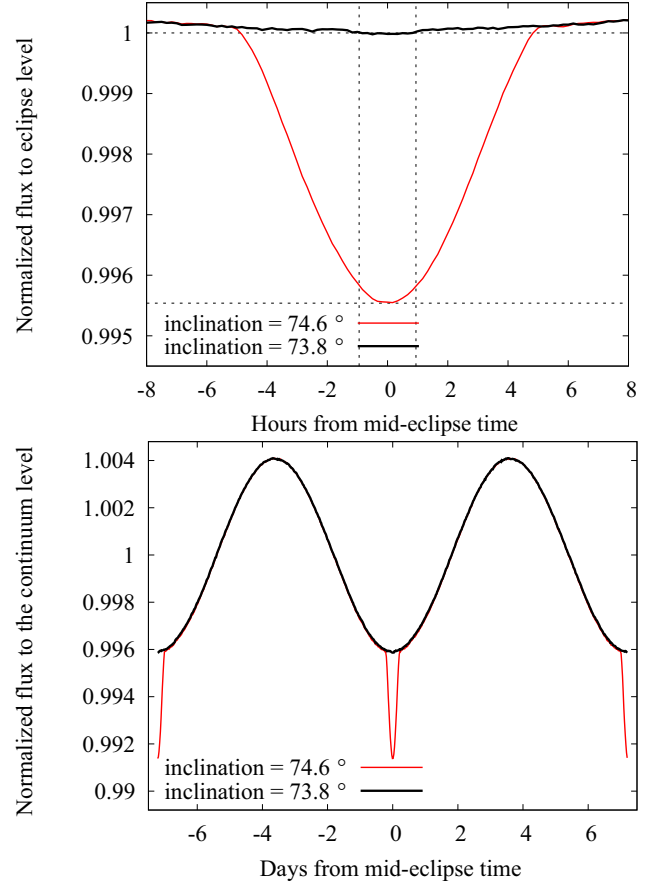


**Fig. 7.** PHOEBE models for two identical G-type stars in a  $\sim 14.4$ -day orbit, for an inclination of  $74.6^\circ$  and  $73.8^\circ$  (red and black continuous lines, respectively). *Top*: zoom-in around the eclipses. Time is given in hours. Horizontal and vertical dashed lines indicate the transit duration and depth, respectively, for visual inspection. *Bottom*: complete orbits, highlighting the continuum flux variability.

**Table 4.** Numerical outcomes for the mass (perturber-to-star) and period (perturber-to-transiting planet) ratios for each of the exterior perturber TTV solutions.

Ratio	Mass-ratio	Period ratio
$<2 : 1$	$1.87 \times 10^{-5}$	1.993
$>3 : 1$	$2.17 \times 10^{-5}$	3.009
$<4 : 1$	$1.18 \times 10^{-5}$	3.991
$<5 : 3$	$2.06 \times 10^{-6}$	1.666
$>2 : 1$	$2.63 \times 10^{-5}$	2.007
$<3 : 2$	$1.23 \times 10^{-6}$	1.498
$>4 : 1$	$1.23 \times 10^{-5}$	4.006
$>5 : 3$	$2.96 \times 10^{-6}$	1.667
$<3 : 1$	$2.31 \times 10^{-5}$	2.994

located, we carried out the usual differential photometry, choosing different apertures centered on KOI-0410, both including and excluding the source. As expected, the increase or decrease in aperture (from 0.9 to 10 arcseconds) changed the overall photometric accuracy of the differential light curves. However, it did not change the shape or depth of the transit. Therefore, as also observed by Bouchy et al. (2011) it is unlikely that the flux drops are caused by a background binary 9 arcseconds away from KOI-0410.

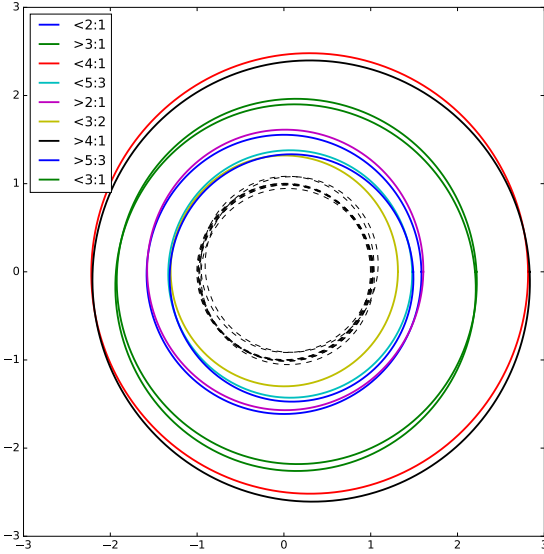


**Fig. 8.** Shapes of the orbits for each of the exterior perturber TTV solutions. The dashed lines represent the orbits for the transiting planet in each case. The axis units are in terms of the semi-major axis of the transiting planet. The exact values for the mass and period ratios are specified in Table 4. The solution just interior to 3:2 is not plotted due to high  $\chi^2$  values.

Furthermore, we investigated the case in which the flux drops were caused by a grazing eclipsing binary in a  $\sim 7.2$ -day orbit, or two similar stars in a  $\sim 14.4$ -day orbit, eclipsing each other every  $\sim 7.2$  days. In both cases, the radial velocity shifts caused by their mutual orbital motion would create a detectable variability, not observed by Bouchy et al. (2011). These authors observed KOI-0410 at two opportunities, at orbital phases close to 0.5 and 0.75, detecting RV shifts inconsistent with the values expected to be caused by two orbiting stars. To examine the scenario of two identical stars in more detail, we simulated two identical G-type stars using the PHysics Of Eclipsing BinariEs<sup>6</sup> (PHOEBE; Prša et al. 2016) code. We assumed stellar radii consistent with G-type stars, with limb-darkening coefficients chosen accordingly and computed as described in von Essen et al. (2013), and we changed the inclination to match both the eclipse duration and depth. On the one hand, for an inclination of 74.6 degrees we matched the eclipse depth ( $\sim 5$  ppt,  $4460.6 \pm 17.8$  parts per million, as reported in the NASA Exoplanet Archive). However, the eclipse duration exceeds the observed time ( $T_{\text{dur}} = 1.899$  h, NASA Exoplanet Archive). On the other hand, decreasing the inclination to 73.8 degrees decreases the eclipse duration considerably (less than 2 h). Nonetheless, the eclipse depth was smaller than  $\sim 0.05$  ppt (see Fig. 7, top). Thus, we could not match both transit depth and duration of KOI-0410.01 to the light curves produced from the PHOEBE models. In addition, both models predict a variability outside eclipse of about  $\sim 1\%$ , which would be clearly visible in the *Kepler* data (Fig. 7, bottom). After visually inspecting the raw data of the 17 quarters and finding no variability modulated with the mentioned periodicity and amplitude, we believe it unlikely that the flux drop is caused by two identical stars in grazing orbits. In addition, the stars should be in exact circular orbits to not show odd/even timing differences, also not observed in the DV report.

Finally, we investigated two additional scenarios: a gravitationally bound hierarchical triple star system and a planet–star

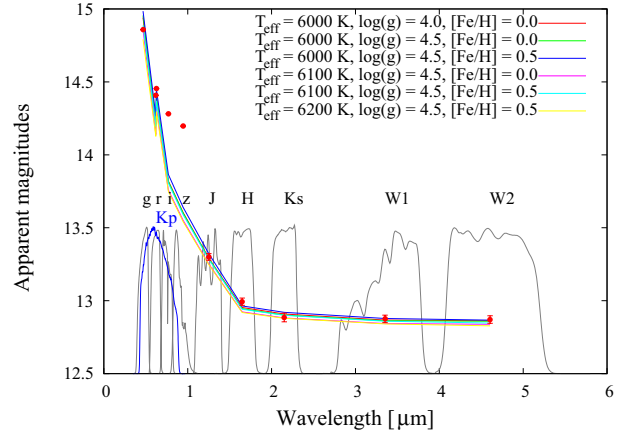


**Fig. 9.** Spectral energy distribution for KOI-0410. The figure shows apparent magnitudes as a function of wavelength, in  $\mu\text{m}$ . Shifted and scaled to match the figure, the filter transmission functions are shown with gray and blue continuous lines. At the top, their respective names: Sloan *g*, *r*, *i* and *z*, *Kepler* band (*Kp*), 2MASS *J*, *H* and *Ks*, and WISE *W1*, *W2*. The first five quantities do not have uncertainties.

system. Here we show some initial results assuming a planet–star system. In this case, the simultaneous MCMC transit fitting of ground- and space-based data suggests a planet solution. Assuming this, the right panel of Fig. 10d shows some initial TTV results obtained from the data acquired during the first and second observing seasons, together with the *Kepler* data. As the figure shows, additional data already scheduled for the 2018 observing season will constrain the solutions even further. The TTV fits were carried out with a novel version of TTVFast (Deck et al. 2014), which utilizes a symplectic integrator developed by Hernandez & Bertschinger (2015) and the universal *Kepler* solver of Wisdom & Hernandez (2015). We computed the TTVs caused by a single, outer perturbing planet near 5:3, 3:2, 2:1, 3:1, and 4:1 period ratios (see Fig. 8 and Table 4), starting the solution just interior and just exterior to each resonance with a super-period (Lithwick et al. 2012) corresponding to  $\approx 3000$  days, following the analysis by Ballard et al. (2011) of *Kepler*-19. We held the mass-ratio of the transiting planet (KOI-0410.01) to the star fixed at  $10^{-5}$ , while we allowed the initial ephemerides and eccentricity vectors of both planets to vary, as well as the mass-ratio of the perturbing planet. We assumed a plane-parallel configuration, and specified the initial orbital elements at  $\text{BJD}_{\text{TDB}} - 2454833 = 130$  days. We optimized the model using a Levenberg–Marquardt solver (Press et al. 1993) with numerically computed, double-sided derivatives. We found relatively good fits near all of these mean-motion resonances, with  $\chi^2$  values ranging from 243 to 290 for 160 degrees of freedom. These chi-square values are uncomfortably large, which may indicate that the timing uncertainties of the planets are underestimated by 20% (in the scenario where the treatment of correlated noise is not sufficient to account for this noise) or created by an astrophysical source, both equally speculative given the data we currently have. The mass ratios of the perturbing planets for these solutions varied from  $10^{-6}$  to  $3 \times 10^{-5}$  (4), while the eccentricities of both planets are modest,  $< 0.15$ . We leave a more detailed description of these results to future work.

To investigate the gravitationally bound hierarchical triple star system scenario, we computed the spectral energy distribution (SED) of KOI-0410. To this end, we used all its available colors, taken from the NASA Exoplanet Archive. These were

<sup>6</sup> <http://phoebe-project.org/>

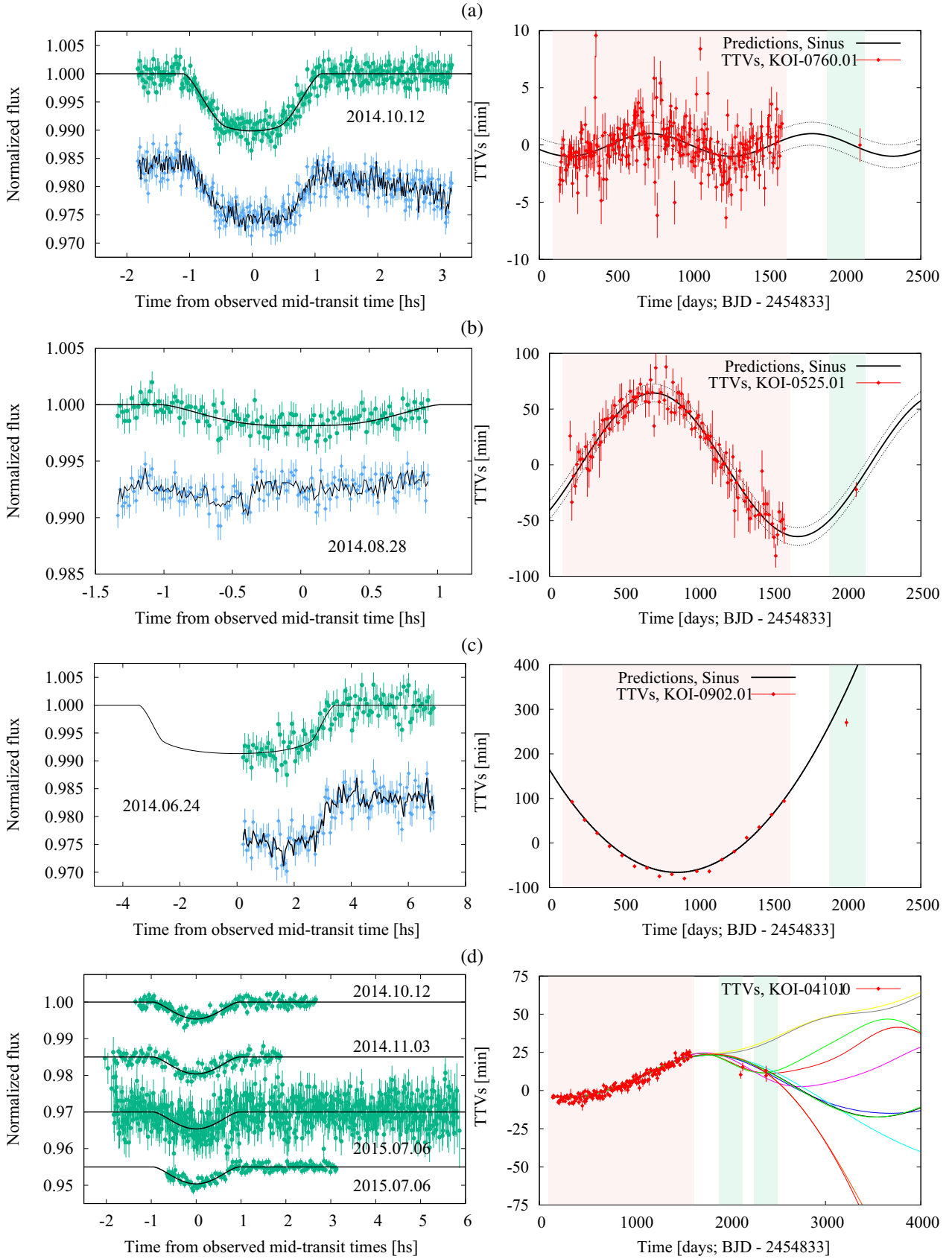


**Fig. 10.** Left panels, from top to bottom: transit observations of KOI-0760.01, KOI-0525.01, KOI-0902.01, and KOI-0410.01. The data are plotted in hours with respect to their best-fit mid-transit times. In all cases green circles show detrended data, along with the best-fit model as black continuous lines. For the first three cases only, the raw data are shown as blue diamonds; the detrending times transit models are overplotted as black lines, shifted down for a better visual comparison, to exemplify our detrending strategy. Right panels: *Kepler* and ground-based TTVs (red diamonds) for the KOIs displayed on the left. Continuous and dashed black and colored lines indicate the predictions and uncertainties, respectively. The red shaded area represents *Kepler* observing time and the green shaded areas represent the 2014 and 2015 observing seasons (March–October).

compared to the “synthetic” colors, which in turn were produced from the PHOENIX stellar models. In particular, when producing the synthetic colors we investigated a wide range of stellar parameters, namely  $T_{\text{eff}} = 6000, 6100, \text{ and } 6200$  kelvin,  $\log(g) = 4.0, 4.5, \text{ and } [\text{Fe}/\text{H}] = -0.5, 0.0$ . If more than one star of similar spectral type conforms to the KOI-0410 system, they should be revealed as an excess in the SED when compared to PHOENIX colors produced from a single star. We find a perfect match between the observed and modeled colors for a star of  $T_{\text{eff}} = 6100$  kelvin,  $\log(g) = 4.5$ , and  $[\text{Fe}/\text{H}] = -0.5$ , close to the values of KOI-0410 reported in the bibliography, with the exception of two photometric bands, namely  $i$  and  $z$  (see Fig. 9). Since all the Sloan measurements do not have uncertainties, during the upcoming 2018 observing season we will observe KOI-0410 again in these photometric bands. At this point we would like to stress that for the KOI-0410 system, the data available cannot really distinguish between the hierarchical triple star system and the planet–star system, not even considering the TTVs. For example, if the binary system was formed by two M-dwarf stars diluted by a G-type star, then the stellar parameters and the radial velocity measurements would be dominated by the latter, while the  $\sim 14.4$ -day period M-dwarf binary (diluted by the G-dwarf) might explain the *Kepler* transits. A G-dwarf star orbiting an M-dwarf binary in a  $\sim 3000$ -day, eccentric orbit might be sufficient to produce the observed TTVs (Borkovits et al. 2003; Agol et al. 2005), causing an ambiguity with the planet–star scenario. We leave a more detailed examination of this scenario to future work.

## 6. Conclusions

KOINet is a large collaboration spanning multiple telescopes across the world aimed at achieving a follow-up coverage of KOIs exhibiting TTVs. We focused our instrumental capabilities initially on 60 KOIs that required additional data to complete a proper characterization or confirmation by means of the TTV technique. A complete list of these KOIs with all the relevant parameters has been provided here.

There are several main challenges associated with the KOIs included in this study: the faintness of their host stars, their shallowness, and their long duration. KOINet presents two fundamental advantages: the access to large telescopes has allowed us to follow up KOIs that are faint ( $\sim 13\text{--}16$  K<sub>p</sub>) and present shallow primary transit events (1–10 ppt), minimizing observational biases. The advantage of ground-based observations is the possibility to acquire short-cadence data, of fundamental relevance for the determination of the mid-transit times. Since the TTVs have already been detected by *Kepler* and most of the systems show a TTV amplitude of several minutes, detecting these offsets has been a straightforward task. The access to large longitudinal coverage has allowed us to have access to several transit occurrences. In addition, since the transit duration grows with the orbital period, for some of the KOIs the transit duration is longer than the astronomical night at a given site. Therefore, more than one site is required to fully observe the transit events. With the observations collected during the 2014 and 2015 observing seasons we have succeeded with our timing precision requirements, we have added new data improving the coverage of the TTV curves of systems where *Kepler* did not register the interaction time fully, and we have built a platform that can observe almost anywhere from the northern hemisphere. Although deriving planetary masses from transit timing observations for more planets to populate the mass-radius diagram is an

ambitious milestone, the work presented here shows that we are on the right track.

*Acknowledgements.* Funding for the Stellar Astrophysics Centre is provided by The Danish National Research Foundation (Grant DNRF106). This research has made use of the NASA Exoplanet Archive, which is operated by the California Institute of Technology, under contract with the National Aeronautics and Space Administration under the Exoplanet Exploration Program. E.A. acknowledges support from NASA Grants NNX13A124G, NNX13AF62G; from National Science Foundation (NSF) grant AST-1615315; and from the NASA Astrobiology Institutes Virtual Planetary Laboratory, supported by NASA under cooperative agreement NNNH05ZDA001C. S.W. acknowledges support from the Research Council of Norway grant 188910 to finance service observing at the NOT, and support for International Team 265 (Magnetic Activity of M-type Dwarf Stars and the Influence on Habitable Extra-solar Planets) funded by the International Space Science Institute (ISSI) in Bern, Switzerland. J.F. acknowledges funding from the German Research Foundation (DFG) through grant DR 281/30-1. Based on observations made with the Nordic Optical Telescope, operated by the Nordic Optical Telescope Scientific Association at the Observatorio del Roque de los Muchachos, La Palma, Spain, of the Instituto de Astrofísica de Canarias. The data presented here were obtained in part with ALFOSC, which is provided by the Instituto de Astrofísica de Andalucía (IAA) under a joint agreement with the University of Copenhagen and NOTSA. Based on observations obtained with the Apache Point Observatory 3.5-m telescope, which is owned and operated by the Astrophysical Research Consortium. Based on observations collected at the German-Spanish Astronomical Center, Calar Alto, jointly operated by the Max-Planck-Institut für Astronomie Heidelberg and the Instituto de Astrofísica de Andalucía (CSIC). This work was supported in part by the Ministry of Education and Science (the basic part of the State assignment, RK no. AAAA-A17-117030310283-7) and by Act no. 211 of the Government of the Russian Federation, agreement no. 02.A03.21.0006. E.H. and I.R. acknowledge support by the Spanish Ministry of Economy and Competitiveness (MINECO) and the Fondo Europeo de Desarrollo Regional (FEDER) through grant ESP2016-80435-C2-1-R, as well as the support of the Generalitat de Catalunya/CERCA programme. E.P., G.T., and Š.M. acknowledge support from the Research Council of Lithuania (LMT) through grant LAT-08/2016. C.D.C. is supported by the Erasmus Mundus Joint Doctorate Program by grant number 2014-0707 from the EACEA of the European Commission. S.E. acknowledges support by the Russian Science Foundation grant No. 14-50-00043 for conducting photometric observations of exoplanets of *Kepler*’s mission. S.I. acknowledges Russian Foundation for Basic Research (project No. 17-02-00542) for support in the processing of the observations. K.P. acknowledges support from the UK Science and Technology Facilities Council through STFC grant ST/P000312/1. H.J.D. acknowledges support by grant ESP2015-65712-C5-4-R of the Spanish Secretary of State for R&D&I (MINECO). KOINet thanks the telescope operators for their invaluable help during some of the observing campaigns at the IAC80 telescope. The IAC80 telescope is operated on the island of Tenerife by the Instituto de Astrofísica de Canarias in the Spanish Observatorio del Teide. C.v.E. is grateful for the invaluable help and contribution of all the telescope operators involved in this work. Eric Agol acknowledges support from a Guggenheim Fellowship.

## References

- Agol, E., Steffen, J., Sari, R., & Clarkson, W. 2005, *MNRAS*, 359, 567  
 Ballard, S., Fabrycky, D., Fressin, F., et al. 2011, *ApJ*, 743, 200  
 Barros, S. C. C., Díaz, R. F., Santerne, A., et al. 2014, *A&A*, 561, L1  
 Barros, S. C. C., Almenara, J. M., Demangeon, O., et al. 2015, *MNRAS*, 454, 4267  
 Becker, A. C., Kundurthy, P., Agol, E., et al. 2013, *ApJ*, 764, L17  
 Becker, J. C., Vanderburg, A., Adams, F. C., Rappaport, S. A., & Schwengeler, H. M. 2015, *ApJ*, 812, L18  
 Borkovits, T., Érdi, B., Forgács-Dajka, E., & Kovács, T. 2003, *A&A*, 398, 1091  
 Borucki, W. J., Koch, D., Basri, G., et al. 2010, *Science*, 327, 977  
 Bouchy, F., Bonomo, A. S., Santerne, A., et al. 2011, *A&A*, 533, A83  
 Carter, J. A., & Winn, J. N. 2009, *ApJ*, 704, 51  
 Carter, J. A., Agol, E., Chaplin, W. J., et al. 2012, *Science*, 337, 556  
 Cash, W. 1979, *ApJ*, 228, 939  
 Claret, A., Hauschildt, P. H., & Witte, S. 2013, *A&A*, 552, A16  
 Cochran, W. D., Fabrycky, D. C., Torres, G., et al. 2011, *ApJS*, 197, 7  
 Collins, K. A., Kielkopf, J. F., & Stassun, K. G. 2017, *AJ*, 153, 78  
 Deck, K. M., Agol, E., Holman, M. J., & Nesvorný, D. 2014, *ApJ*, 787, 132  
 Eastman, J., Siverd, R., & Gaudi, B. S. 2010, *PASP*, 122, 935  
 Fabrycky, D. C., Ford, E. B., Steffen, J. H., et al. 2012, *ApJ*, 750, 114  
 Fabrycky, D. C., Lissauer, J. J., Ragozzine, D., et al. 2014, *ApJ*, 790, 146  
 Fang, J., & Margot, J.-L. 2012, *ApJ*, 761, 92

- Ford, E. B., & Holman, M. J. 2007, *ApJ*, **664**, L51
- Ford, E. B., Fabrycky, D. C., Steffen, J. H., et al. 2012a, *ApJ*, **750**, 113
- Ford, E. B., Ragozzine, D., Rowe, J. F., et al. 2012b, *ApJ*, **756**, 185
- Fukui, A., Narita, N., Tristram, P. J., et al. 2011, *PASJ*, **63**, 287
- Fukui, A., Narita, N., Kawashima, Y., et al. 2016, *ApJ*, **819**, 27
- Gibson, N. P., Pollacco, D., Simpson, E. K., et al. 2009, *ApJ*, **700**, 1078
- Gillon, M., Jehin, E., Lederer, S. M., et al. 2016, *Nature*, **533**, 221
- Hadden, S., & Lithwick, Y. 2014, *ApJ*, **787**, 80
- Hadden, S., & Lithwick, Y. 2017, *AJ*, **154**, 5
- Hernandez, D. M., & Bertschinger, E. 2015, *MNRAS*, **452**, 1934
- Holczer, T., Mazeh, T., Nachmani, G., et al. 2016, *ApJS*, **225**, 9
- Holman, M. J., & Murray, N. W. 2005, *Science*, **307**, 1288
- Holman, M. J., Fabrycky, D. C., Ragozzine, D., et al. 2010, *Science*, **330**, 51
- Howell, S. B. 2006, *Handbook of CCD Astronomy*, eds. R. Ellis, J. Huchra, S. Kahn, G. Rieke, & P. B. Stetson (Cambridge, UK: Cambridge University Press)
- Jiang, I.-G., Lai, C.-Y., Savushkin, A., et al. 2016, *AJ*, **151**, 17
- Jones, E., Oliphant, T., Peterson, P., et al. 2001, *SciPy: Open source scientific tools for Python*, <http://www.scipy.org/citing.html>
- Jontof-Hutter, D., Rowe, J. F., Lissauer, J. J., Fabrycky, D. C., & Ford, E. B. 2015, *Nature*, **522**, 321
- Jontof-Hutter, D., Ford, E. B., Rowe, J. F., et al. 2016, *ApJ*, **820**, 39
- Kipping, D. M. 2010, *MNRAS*, **408**, 1758
- Kipping, D. M., Nesvorný, D., Buchhave, L. A., et al. 2014, *ApJ*, **784**, 28
- Kjeldsen, H., & Frandsen, S. 1992, *PASP*, **104**, 413
- Koch, D. G., Borucki, W. J., Basri, G., et al. 2010, *ApJ*, **713**, L79
- Kundurthy, P., Barnes, R., Becker, A. C., et al. 2013, *ApJ*, **770**, 36
- Laughlin, G., & Chambers, J. E. 2001, *ApJ*, **551**, L109
- Lissauer, J. J., Fabrycky, D. C., Ford, E. B., et al. 2011a, *Nature*, **470**, 53
- Lissauer, J. J., Ragozzine, D., Fabrycky, D. C., et al. 2011b, *ApJS*, **197**, 8
- Lissauer, J. J., Dawson, R. I., & Tremaine, S. 2014, *Nature*, **513**, 336
- Lithwick, Y., Xie, J., & Wu, Y. 2012, *ApJ*, **761**, 122
- Maciejewski, G., Dimitrov, D., Neuhäuser, R., et al. 2011, *MNRAS*, **411**, 1204
- Maciejewski, G., Dimitrov, D., Seeliger, M., et al. 2013, *A&A*, **551**, A108
- Malhotra, R., Black, D., Eck, A., & Jackson, A. 1992, *Nature*, **356**, 583
- Mallonn, M., Nascimbeni, V., Weingrill, J., et al. 2015, *A&A*, **583**, A138
- Mandel, K., & Agol, E. 2002, *ApJ*, **580**, L171
- Mazeh, T., Nachmani, G., Holczer, T., et al. 2013, *ApJS*, **208**, 16
- Mislis, D., Mancini, L., Tregloan-Reed, J., et al. 2015, *MNRAS*, **448**, 2617
- Mordasini, C., Alibert, Y., Georgy, C., et al. 2012, *A&A*, **547**, A112
- Mukadam, A. S., Owen, R., Mannery, E., et al. 2011, *PASP*, **123**, 1423
- Nespral, D., Gandolfi, D., Deeg, H. J., et al. 2017, *A&A*, **601**, A128
- Nesvorný, D., & Morbidelli, A. 2008, *ApJ*, **688**, 636
- Nesvorný, D., Kipping, D., Terrell, D., et al. 2013, *ApJ*, **777**, 3
- Nesvorný, D., Kipping, D., Terrell, D., & Feroz, F. 2014, *ApJ*, **790**, 31
- Ofir, A., Dreizler, S., Zechmeister, M., & Husser, T.-O. 2014, *A&A*, **561**, A103
- Patil, A., Huard, D., & Fonnesbeck, C. J. 2010, *J. Stat. Softw.*, **35**, 1
- Peale, S. J. 1993, *AJ*, **105**, 1562
- Petrucci, R., Jofré, E., Melita, M., Gómez, M., & Mauas, P. 2015, *MNRAS*, **446**, 1389
- Press, W. H., Teukolsky, S. A., Vetterling, W. T., & Flannery, B. P. 1993, *Numerical Recipes in FORTRAN; The Art of Scientific Computing*, 2nd edn. (New York, USA: Cambridge University Press)
- Prša, A., Conroy, K. E., Horvat, M., et al. 2016, *ApJS*, **227**, 29
- Raetz, S., Maciejewski, G., Seeliger, M., et al. 2015, *MNRAS*, **451**, 4139
- Rasio, F. A., Nicholson, P. D., Shapiro, S. L., & Teukolsky, S. A. 1992, *Nature*, **355**, 325
- Rivera, E. J., Laughlin, G., Butler, R. P., et al. 2010, *ApJ*, **719**, 890
- Seager, S. 2010, *Exoplanet Atmospheres: Physical Processes* (NJ: Princeton University Press)
- Southworth, J., Hinse, T. C., Jørgensen, U. G., et al. 2009, *MNRAS*, **396**, 1023
- Stefansson, G., Mahadevan, S., Hebb, L., et al. 2017, *ApJ*, **848**, 9
- Steffen, J. H., & Agol, E. 2005, *MNRAS Lett.*, **364**, L96
- Steffen, J. H., Fabrycky, D. C., Ford, E. B., et al. 2012a, *MNRAS*, **421**, 2342
- Steffen, J. H., Ragozzine, D., Fabrycky, D. C., et al. 2012b, *Proc. Nat. Acad. Sci.*, **109**, 7982
- von Essen, C., Schröter, S., Agol, E., & Schmitt, J. H. M. M. 2013, *A&A*, **555**, A92
- von Essen, C., Cellone, S., Mallonn, M., Tingley, B., & Marcussen, M. 2016, *A&A*, submitted, [[arXiv:1607.03680](https://arxiv.org/abs/1607.03680)]
- Winn, J. N., Holman, M. J., Torres, G., et al. 2008, *ApJ*, **683**, 1076
- Wisdom, J., & Hernandez, D. M. 2015, *MNRAS*, **453**, 3015
- Wolszczan, A. 1994, *Science*, **264**, 538
- Xie, J.-W. 2013, *ApJS*, **208**, 22
- Xie, J.-W. 2014, *ApJS*, **210**, 25
- Young, A. T., Genet, R. M., Boyd, L. J., et al. 1991, *PASP*, **103**, 221
- 
- <sup>1</sup> Stellar Astrophysics Centre, Ny Munkegade 120, 8000 Aarhus, Denmark
- <sup>2</sup> Institut für Astrophysik, Georg-August-Universität Göttingen, Friedrich-Hund-Platz 1, 37077 Göttingen, Germany  
e-mail: [cessen@phys.au.dk](mailto:cessen@phys.au.dk)
- <sup>3</sup> Department of Earth and Planetary Sciences, Weizmann Institute of Science, Rehovot 76100, Israel
- <sup>4</sup> Astronomy Department, University of Washington, Seattle, WA 98195, USA
- <sup>5</sup> Institut d'Astrophysique de Paris, 98 bis Boulevard Arago, 75014 Paris, France
- <sup>6</sup> NASA Astrobiology Institute, Virtual Planetary Laboratory Team, Seattle, Washington, USA
- <sup>7</sup> Instituto de Astronomía, UNAM, Campus Ensenada, Carretera Tijuana-Ensenada km 103, 22860 Ensenada, B.C. México
- <sup>8</sup> Rosseland Centre for Solar Physics, University of Oslo, PO Box 1029 Blindern, 0315 Oslo, Norway
- <sup>9</sup> Institute of Theoretical Astrophysics, University of Oslo, PO Box 1029 Blindern, 0315 Oslo, Norway
- <sup>10</sup> School of Physics and Astronomy, Monash Centre for Astrophysics (MoCA), Monash University, Clayton, Victoria 3800, Australia
- <sup>11</sup> Instituto de Astrofísica de Canarias, C/ Vía Láctea s/n, 38205 La Laguna, Tenerife, Spain
- <sup>12</sup> Universidad de La Laguna, Dept. de Astrofísica, 38206 La Laguna, Tenerife, Spain
- <sup>13</sup> Aix-Marseille Université, CNRS, LAM, Laboratoire d'Astrophysique de Marseille, Marseille, France
- <sup>14</sup> Yunnan Observatories, Chinese Academy of Sciences, PO Box 110, Kunming 650216, Yunnan Province, PR China
- <sup>15</sup> Institut de Ciències de l'Espai (IEEC-CSIC), C/Can Magrans s/n, Campus UAB, 08193 Bellaterra, Spain
- <sup>16</sup> Observatori del Montsec (OAdM), Institut d'Estudis Espacials de Catalunya (IEEC), C/Gran Capità 2-4, Edif. Nexus, 08034 Barcelona, Spain
- <sup>17</sup> School of Geosciences, Raymond and Beverly Sackler Faculty of Exact Sciences, Tel Aviv University, Tel Aviv 6997801, Israel
- <sup>18</sup> Astrophysics Research Centre, Queen's University Belfast, Belfast BT7 1NN, UK
- <sup>19</sup> Leibniz-Institut für Astrophysik Potsdam, An der Sternwarte 16, 14482 Potsdam, Germany
- <sup>20</sup> Hamburg Observatory, Hamburg University, Gojenbergsweg 112, 21029 Hamburg, Germany
- <sup>21</sup> Institute for Astronomy, Astrophysics, Space Applications and Remote Sensing, National Observatory of Athens, Metaxa & Vas. Pavlou St., Penteli, Athens, Greece
- <sup>22</sup> Dipartimento di Fisica e Scienze della Terra, Università degli Studi di Ferrara, via Saragat 1, 44122 Ferrara, Italy
- <sup>23</sup> Department of Astronomy & Astrophysics, University of Chicago, Chicago, IL 60637, USA
- <sup>24</sup> Institute of Theoretical Physics and Astronomy, Vilnius University, Sauletekio 3, 10257 Vilnius, Lithuania
- <sup>25</sup> Indian Institute of Astrophysics, Koramangala II block, Bangalore 560034, India
- <sup>26</sup> Instituto de Astronomía, Universidad Católica del Norte, Av. Angamos, 0610 Antofagasta, Chile
- <sup>27</sup> Central Astronomical Observatory at Pulkovo of Russian Academy of Sciences, Pulkovskoje shosse d. 65, St. Petersburg 196140, Russia
- <sup>28</sup> Special Astrophysical Observatory, Russian Academy of Sciences, Nizhnyj Arkhyz 369167, Russia
- <sup>29</sup> Kourovka Astronomical Observatory of Ural Federal University, Mira Str. 19, 620002 Yekaterinburg, Russia